UCLA
UCLA Previously Published Works

Title

Publisher Correction: Elastomeric sensor surfaces for high-throughput single-cell force cytometry.

Permalink

https://escholarship.org/uc/item/4t47f1cj

Journal

Nature biomedical engineering, 2(4)

ISSN

2157-846X

Authors

Pushkarsky, Ivan
Tseng, Peter
Black, Dylan
et al.

Publication Date

2018-04-01

DOI

10.1038/s41551-018-0207-0

Peer reviewed

eScholarship.org Powered by the California Digital Library
University of California

Elastomeric sensor surfaces for high-throughput single-cell force cytometry

Ivan Pushkarsky, [1]

Peter Tseng, [1,2]

Dylan Black, [1]

Bryan France, [3]

Lyndon Warfe, [1]

Cynthia J. Koziol-White, [4]

William F. Jester , Jr [4]

Ryan K. Trinh, [5]

Jonathan Lin, [1]

Philip O. Scumpia, [6]

Sherie L. Morrison, [5]

Reynold A. Panettieri, Jr [4]

Robert Damoiseaux, [3,7]

Dino Di Carlo, [1✉,3,8]

Email: dicarlo@seas.ucla.edu

[1] Department of Bioengineering, University of California, Los Angeles, Los Angeles, CA, USA

[2] Department of Electrical Engineering and Computer Science, University of California, Los Angeles, Irvine, CA, USA

[3] California NanoSystems Institute, University of California, Los Angeles, Los Angeles, CA, USA

[4] Rutgers Institute for Translational Medicine and Science, Child Health Institute, Rutgers University, New Brunswick, New Jersey, United States

[5] Department of Microbiology, Immunology and Molecular Genetics and The Molecular Biology Institute, University of California, Los Angeles, Los Angeles, CA, USA

[6] Division of Dermatology, David Geffen School of Medicine, University of California, Los Angeles, Los Angeles, CA, USA

[7] Department of Molecular and Medicinal Pharmacology, University of California, Los Angeles, Los Angeles, CA, USA

[8] Department of Mechanical Engineering, University of California, Los Angeles, Los Angeles, CA, USA

Received: 7 April 2017 / Accepted: 9 January 2018

Abstract

As cells with aberrant force-generating phenotypes can directly lead to disease, cellular force-generation mechanisms are high-value targets for new therapies. Here, we show that single-cell force sensors embedded in elastomers enable single-cell force measurements with ~100-fold improvement in throughput than was previously possible. The microtechnology is scalable and seamlessly integrates with the multi-well plate format, enabling highly parallelized time-course studies. In this regard, we show that airway smooth muscle cells isolated from fatally asthmatic patients have innately greater and faster force-generation capacity in response to stimulation than healthy control cells. By simultaneously tracing agonist-induced calcium flux and contractility in the same cell, we show that the calcium level is ultimately a poor quantitative predictor of cellular force generation. Finally, by quantifying phagocytic forces in thousands of individual human macrophages, we show that force initiation is a digital response (rather than a proportional one) to the proper immunogen. By combining mechanobiology at the single-cell level with high-throughput capabilities, this microtechnology can support drug-discovery efforts for clinical conditions associated with aberrant cellular force generation.

AQ1

AQ2

AQ3

A microtechnology involving force sensors embedded in elastomers for cell culture enables the high-throughput measurement of single-cell force generation from contractile cells in a scalable and highly parallelized manner.

Ivan Pushkarsky and Peter Tseng contributed equally to this work.

Main

Cell-generated mechanical forces, which normally fulfil essential biological roles at both the cellular level (such as mechanotransduction[1], migration[2], cytokinesis[3], immune processes[4] and vasoregulation[5]) and the tissue level (such as tone maintenance and concerted contractions) can at times become dysregulated, leading to diseased anatomical states or loss of function. Abnormally high force generation underlies bronchoconstriction[6] in asthma, hypertensive vasoconstriction and stroke[7], and muscle spasms, and is also involved in fibrotic tissue stiffening[8] and in the pathogenesis of cancer[9]. Conversely, the inability of cells to generate force describes the phenotypic basis for cardiac insufficiency and congenital defects such as X-linked neutropenia and muscular dystrophy. Furthermore, undesired vasodilation in the brain has been identified as the physiological trigger for migraine pain[10]. Therefore, cellular force generation can serve as a useful measure for evaluating disease state and provides a valuable therapeutic target.

AQ4

AQ5

For several therapeutic indications, existing treatments promote the relaxation of cell shortening through established molecular pathways. However, the coupling of the molecular pathways to the contractile force remains poorly understood. Because conventional therapies induce severe side effects and tolerance development or are simply ineffective, new approaches are needed that act specifically and effectively on mechanical force transduction. A scalable cellular force cytometer of general use that could rapidly evaluate large screening libraries would accelerate drug-development efforts and anchor research in force biology.

Existing techniques for performing these measurements suffer from strict trade-offs between the quality of the data on the one hand and throughput and ease of use on the other. Traction force microscopy (TFM)[11, 12] and elastomeric micropost array[13] assays can resolve sub-cellular forces, but require laborious manual steps that have limited throughput to only a few dozen cells in a typical experiment[14, 15, 16, 17]. TFM serially implemented in a microtiter plate format increased throughput but lost its single-cell resolution, instead reporting a noise-prone, bulk 'response-ratio' measurement[11] that overlooked clinically important sub-populations, such as the highly contractile platelets present in patients with normal clotting function[18]. A concept combining TFM and fluorescent micropatterns was also proposed, but was ultimately limited to proof-of-principle due to practical fabrication challenges[19]. To address the need to scale up data acquisition, both in terms of cell numbers and temporal resolution, we introduce an integrated biosensor material comprising fluorescently labelled elastomeric contractible surfaces (FLECS) for making single-cell force measurements at throughputs ~100-fold higher than was previously possible.

In the FLECS system, each cell adhering to one of thousands of uniform adhesive and fluorescent micropatterns generates comparable mechanical forces onto the underlying elastomeric film and produces unique, well-calibrated displacements at their respective micropatterns' peripheries (Fig. 1a and Supplementary Videos 1 and 2), which can easily be quantified using image analysis algorithms (Fig. 1c). By combining micro-contact printing of proteins with sacrificial layers, we can stably encode micropatterns consisting of any biomolecule bearing free amine or thiol groups into a silicone elastomer without using costly linkers, resulting in uniform micropatterns that are unaffected by material stiffness (Supplementary Fig. 1). This allows us to simulate diverse tissue environments, which, in turn, can elicit a wide range of measurable force-generating behaviours, from basal smooth muscle tone to phagocytosis. Importantly, in a multi-well plate format, FLECS achieves a substantial degree of parallelization without linear increases in fabrication labour. The 96-well plate embodiment (containing >6,000 70 μm 'X' patterns per well) is natively compatible with existing automation and screening infrastructures (that is, liquid-handling robotics, plate-handling robotics and high-content imaging systems) and offers a practical solution to performing highly parallelized assays and other general experiments that were previously too costly or cumbersome.

Fig. 1

Operational principles of the general-use FLECS force cytometer.

a, Top: technology schematic showing cells adhered to functionalized adhesive micropatterns embedded into a thin glass-supported elastomeric film. Left: top view showing multiple pattern shapes and a blow-up of a cell contracting an 'X' pattern and inwardly displacing its terminals. Middle: overlay of fluorescent patterns and phase contrast images of adhered contracting cells. Right: time-lapsed images of a contracting cell and the underlying micropattern. Scale bars: 25 μm. **b**, Well-plate implementation. **c**, Image analysis workflow. Input: image sets of the micropatterns (set 1) and stained cell nuclei (set 2). Processing: the algorithm (1) identifies and measures all micropatterns in image set 1, (2) cross-references the positions of each micropattern in image set 2 and (3) determines whether 0, 1 or >2 nuclei (that is, cells) are present (see Supplementary Fig. 2). Output: mean centre-to-terminal displacements of the micropatterns containing a single nucleus (that is, one cell) are compared with the median of the corresponding measurement of all undisplaced patterns containing zero nuclei (that is, unoccupied patterns) and the differences are plotted as a horizontal histogram. Scale bars: 35 μm.

AQ6

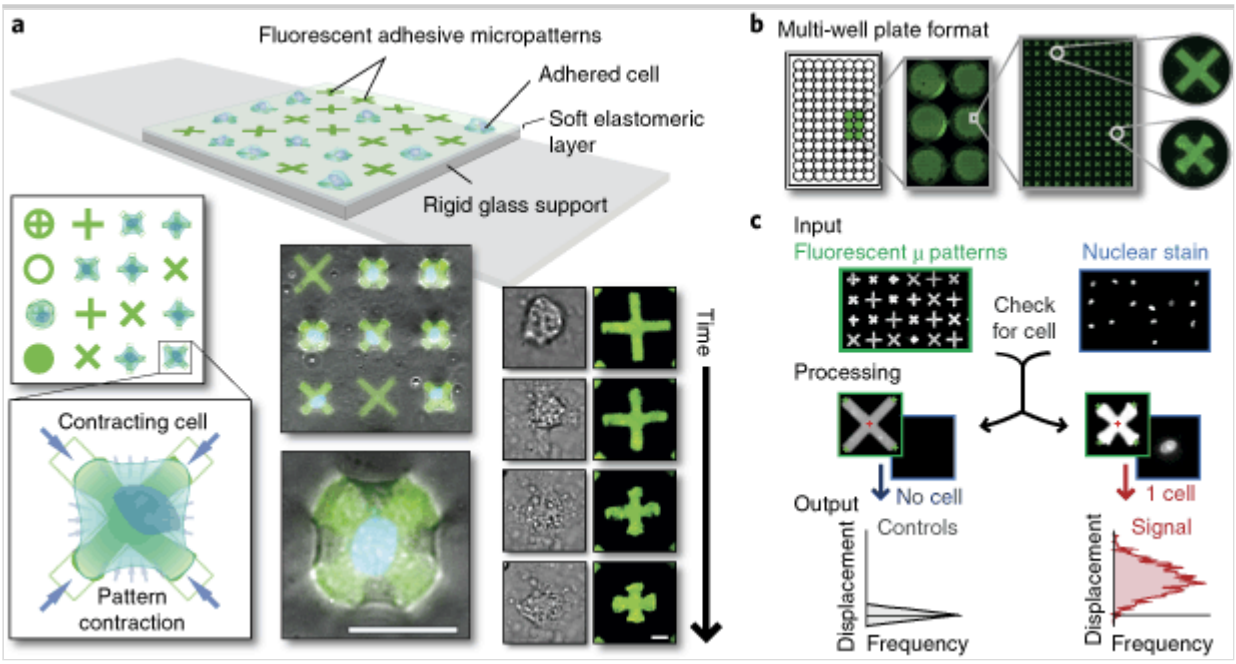

Results

Whole-cell contractility measurements resolve population-wide contractile differences

FLECS provides whole-cell contractility measurements. To show that this level of resolution is sufficient for detecting population-wide contractile differences, we

assayed multi-potent human mesenchymal stem cells (hMSCs), which are known to exert large contractile forces and to interrogate mechanical cues in their environment[20, 21] and differentiated progeny. hMSCs spread uniformly to occupy 70 μm fibronectin 'X' patterns, forming dense actin stress fibres (Fig. 2b and Supplementary Fig. 3). Regardless of the tissue of origin, hMSCs in a multi-potent state produced significantly higher steady-state micropattern displacements than either set of differentiated hMSCs, suggesting greater force generation (Fig. 2a). A previous study reported high forces in differentiating hMSCs that peaked in the first day of culture but declined over the following seven days[22]. Our results support this earlier conclusion as they reveal significantly lower forces in MSCs following longer differentiation times (that is, at 14 days, as in our experiment) and indicate that sub-cellular resolution is not necessary for population-wide cellular force cytometry. Furthermore, because FLECS assays all cells present in a sample without pre-selection in one automated procedure, we obtained data for 180 to >1,500 cells per condition (rather than 13–62 cells, as was presented in the previous study) and identified a smaller sub-population of weakly contractile cells in each multi-potent stem cell sample.

Fig. 2

Whole-cell contractility resolves contractile changes with differentiation and drug treatment.

a, Primary human adipose- or bone-marrow-derived MSCs exhibited much higher contractile responses than either committed lineage 8 h post-seeding. Non-contractile sub-populations were seen among the MSCs, indicating heterogeneity and potentially low purity that resulted from standard separation methods. '*n*' represents the number of cells. A typical contracted pattern approximately representing the median case from each distribution is shown below. **b**, Overlays of fluorescent images of contracted patterns (green), phalloidin-stained actin (red) and nuclei (blue) of adipose-derived multi-potent MSCs showing three instances of cells fully spread over the patterns and actin stress fibres that route stresses to the vertices of the 'X' patterns. Scale bars: 25 μm. **c**, Representative distributions of single-cell responses to increasing doses of blebbistatin. Plots comprise pooled data from four technical replicates of each condition. **d**, Dose-response curve over 3 decades in which we identify an IC_{50} of 2.61 μM. Error bars represent s.e.m. '*n*' represents number of cells in each distribution. The Kruskal–Wallis test for non-parametric data was used to perform statistical analyses on the contractile distributions with significance defined as $P < 0.05$. Scale bars: 35 μm.

AQ7

AQ8

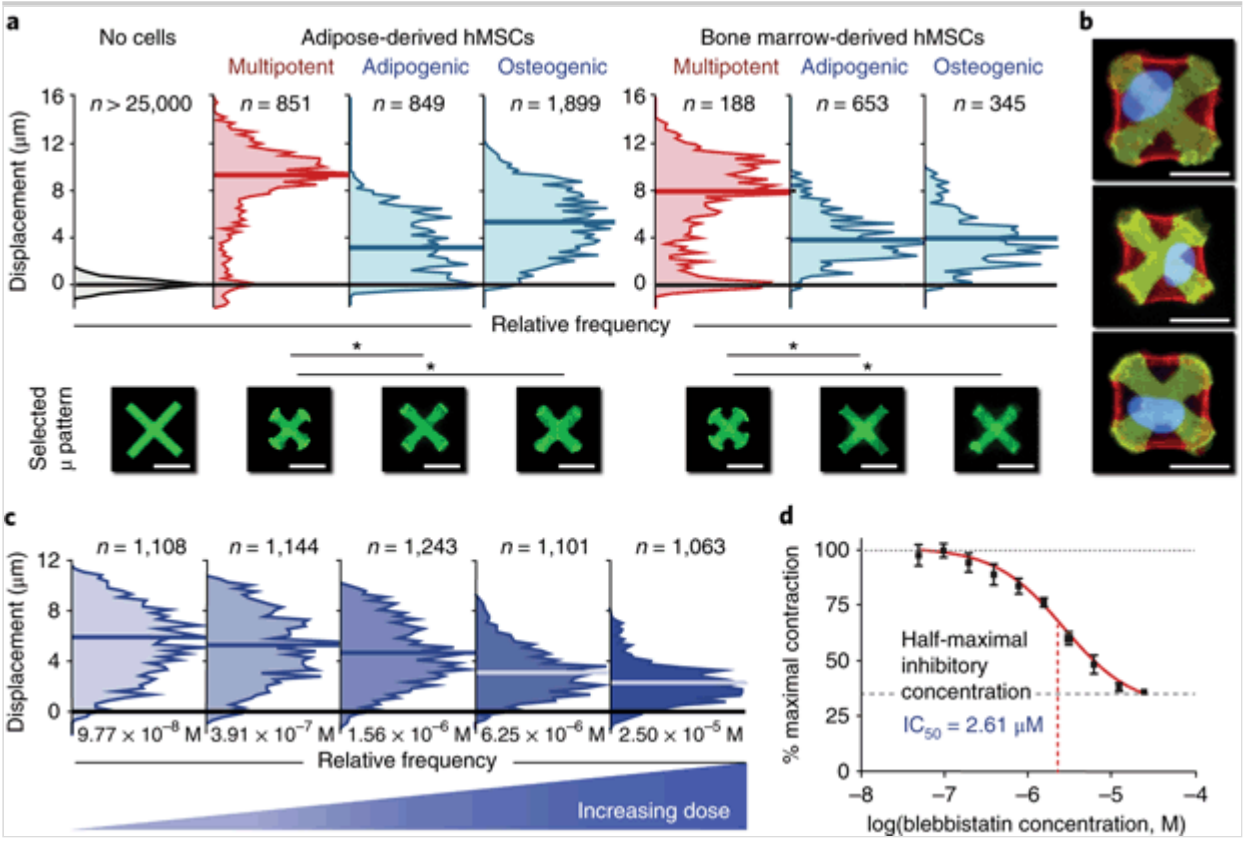

Additional experiments using FLECS were performed to characterize and compare whole-cell contractility for three types of primary human smooth muscle cells (SMCs)—bronchial SMCs, aortic SMCs and uterine SMCs. These cells were observed to uniformly spread over and contract thousands of 70 μm 'X' patterns, producing measurable displacements that were on average greater for aortic SMCs and uterine SMCs than for bronchial SMCs, suggesting higher native force generation by those cells in the absence of stimuli (Supplementary Fig. 4). A larger sub-population of weakly contracting cells was also identified in the uterine SMC distribution, perhaps due to the relative difficulty of isolating pure populations from this complex tissue. These experiments further support the suitability of FLECS for studying the force biology of a variety of adherent tissue cells.

Considering the multitude of disorders arising from abnormal SMC contractility, including asthma, hypertension and bowel disease[23], technology for rapid force-phenotyping of large SMC populations would be invaluable for research and drug-development purposes. In support of this idea, we tested whether whole-cell contractility measurements obtained with FLECS provide sufficient resolution for performing functional phenotypic screens of modulators of cellular force, and

whether accurate quantitative characterization of drug compounds can be achieved. To do so, we titrated the myosin II inhibitor blebbistatin using contracting primary human airway smooth muscle (HASM) following a 10-step, twofold dilution scheme and vehicle controls with 4 technical replicates for each (equating to 44 independent measurements) on a single functionalized 96-well plate (Fig. 2c). As expected, the addition of this tool compound produced a restorative effect on the cell-contracted micropatterns (Supplementary Video 3), which was dose dependent. We observed low variability across replicates and calculated an IC_{50} of 2.61 μM, which matches previously reported values[24, 25] (Fig. 2d). These results show that automating (and scaling) the FLECS assay is feasible and yields robust readouts. As such, we expect the FLECS well-plate to facilitate automated screens of large drug libraries to help identify new candidates for correcting malfunctioning cellular contractility. The single-cell resolution should also help reveal any non-Gaussian responses to modulators at the population level.

Airway SMCs isolated from donors with asthma inherently generate higher forces

Used together with laboratory automation equipment, the well-plate implementation of FLECS provides new opportunities to perform highly parallelized and multi-faceted studies of force generation with high precision and fine temporal resolution. Here, we harnessed these capabilities to thoroughly evaluate the functional contractile profiles of primary HASM cells isolated from patients with fatal asthma and compared them with cells from patients who were age-, race- and gender-matched without asthma. Researchers in the field have supposed that innate differences in force generation should exist between the two sets, yet the various aspects of this phenotype have never been compared directly using a single method or with large quantities of cells. Although a previous study compared this mechanophenotype between patient cells using TFM for a number of cells at baseline, the traction moments were not normalized to the cell-spread area, which is known to dictate traction forces, and contractility could not be assessed following dosing with agonists[26]. Moreover, the comparative responsiveness to asthma treatments has not previously been compared between normal and diseased HASM cells. Here, we aimed to provide a definitive report on whether force generation was indeed inherently greater in asthma HASM cells using a single measurement methodology and evaluating both tone and responsiveness in thousands of the same cells. For this study, we evaluated (1) the basal cell tone, (2) contractile responsiveness to treatment with a bronchoconstrictor and (3) the responsiveness to attempted rescue from bronchoconstriction using the asthma standard-of-care β2-

adrenoceptor agonist formoterol in the same cells. Six unique patient samples were taken from each group (Fig. 3).

Fig. 3

Parallel study of fatal asthma and non-asthma patient-derived airway SMCs.

a, Experimental workflow. Patient-derived HASM cell lines ($n = 12$) were seeded into 8 wells each in a FLECS well-plate and a baseline image was taken. All cells were then treated with the contractile agonist bradykinin (BK; 10 μM final concentration) and imaged for 16 min at 4-min intervals. Half of all cells were treated with 50 μM formoterol and the other half were treated with DMSO vehicle. Cells were imaged for an additional 20 min at 4-min intervals and finally 10 min later. **b**, Distributions of responsive cells from a representative patient. The distribution shifts upwards following BK treatment and is halted by formoterol. **c**, Median values of the evolving contractile distributions for each of 12 patient cell lines with or without formoterol treatment. Each data point in each trace comprises an average of four separate well measurements on the well-plate. **d**, Pair-wise comparison of age-, race- and gender-matched patients with and without asthma. The first age listed is for the normal patient, while the second is for the asthmatic patient. The letters denote race and gender. The full characteristics for all patient donors are listed in Supplementary Table 1. In general, HASM cells from asthma patients exhibited greater tone and/or contraction following stimulation. A one-tailed Student's *t*-test was performed on the patient pairs in **d**. $*P < 0.05$; $***P < 0.001$. Error bars represent s.e.m. AA, African American; C, Caucasian; F, female; M, male.

AQ11

AQ12

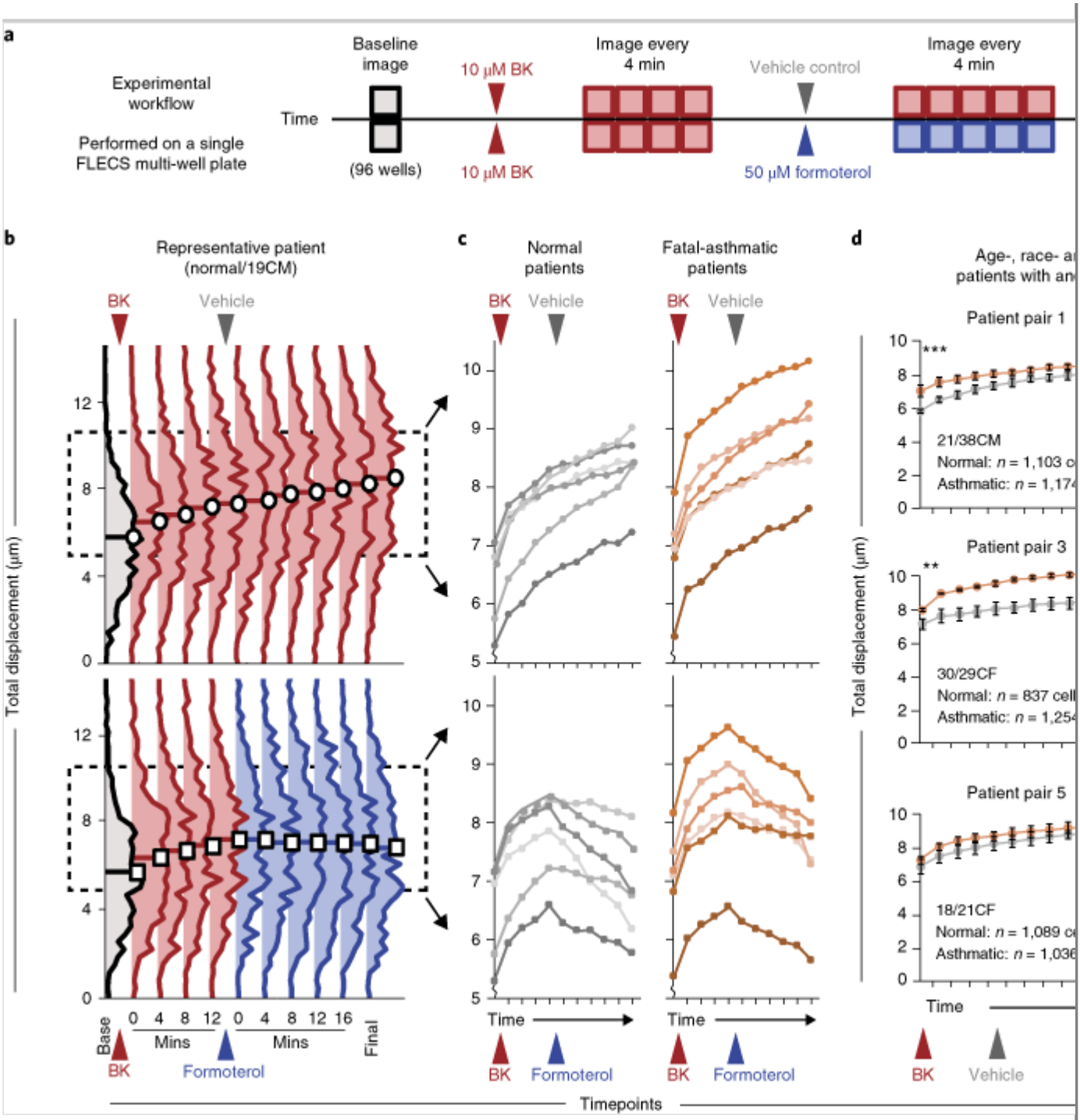

AQ9

AQ10

HASM cells from asthmatic patients contracted patterns with a higher baseline tone than cells from healthy patients. To first evaluate tone, the 12 HASM cell lines were seeded into 8 wells, each within 3 FLECS multi-well plates. Each of these was assembled with independently mixed batches of silicone elastomer. Following adhesion and serum starvation, all wells were imaged to obtain basal (tonic) contraction levels for the 12 cells lines. The trends in tonic contraction between the

12 cell populations were conserved across the three samples, and the minor inter-well-plate variability was significantly less than the inter-donor variability we observed, indicating that the method reliably discerns biological differences (Supplementary Fig. 5). Here, we observed that the asthma HASM cells exhibited, on average, higher tone than the non-asthma HASM cells. When compared as two pooled groups, the median basal tone of all asthma HASM cells was statistically greater than the median basal tone of non-asthma HASM cells (Fig. 4a).

Fig. 4

Collective comparisons of all asthma versus non-asthma HASM cells.

a–**d**, Each data point represents the median value of an individual well measurement. All wells ($n = 96$) were compared in **a**, only wells that received the vehicle ($n = 48$) were compared in **b** and **c**, and only wells that received formoterol ($n = 48$) were compared in **d**. The tone was statistically greater for asthmatic HASM cells. The initial rate of response to bradykinin (BK) was also greater for asthmatic cells. However, the long-term time response over the course of the experiment and rescue via formoterol were similar for the two groups. A one-tailed Student's *t*-test was performed on pooled groups. NS, not significant.

AQ14

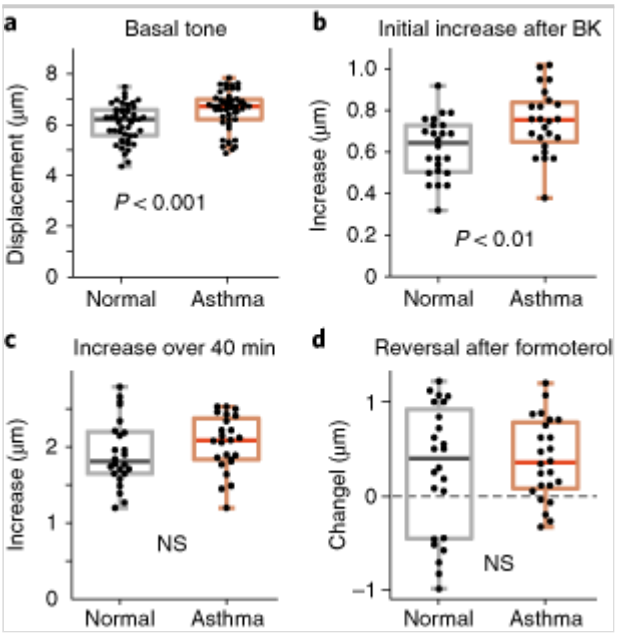

AQ13

Immediately after imaging cells in their tonic contracted state, we treated them all with the contractile agonist bradykinin at a final concentration of 10 μM. We had

previously observed bradykinin as well as endothelin-1—both of which are molecules that have been impugned in asthma—to promote significant contraction in primary HASM (Supplementary Videos 4 and 5). Following treatment, all 96 sites were re-imaged once every 4 min for 16 min, at which point the plate was removed from the imager and half the wells received 50 μM formoterol, while the other half received vehicle (1% dimethyl sulfoxide (DMSO)). The plate was replaced and all sites were imaged for another 20 min at 4-min intervals before a final time point was recorded 10 min later. Contractility for each of the ~31,000 cells was tracked over time and cells exhibiting increased contraction at 16 min relative to baseline were selected for further analysis (~72% of cells on average).

We tracked the evolving contractile distributions for all selected cells (Fig. 3b) and found that the distributions showed robust upwards shifts following treatment with bradykinin that were un-attenuated following the addition of vehicle, but were halted or reversed following treatment with formoterol. The median contractility value of each cell population was tracked over the course of pharmacological treatment (Fig. 3c) and it was observed that for five of six pairs of age-, race- and gender-matched patients with or without fatal asthma, the asthmatic patients' cells exhibited either greater tone, greater bradykinin-induced contraction or both (Fig. 3d). In four of these cases, the differences were statistically significant. One asthma line (asthma patient 6) displayed lower contraction in all respects than its healthy patient counterpart. We conclude that, in general, HASM cells isolated from fatal-asthmatic patients innately generate greater force than cells isolated from their healthy counterparts.

The acute contractile response to the agonist also appeared significantly accelerated in fatal-asthmatic patient-derived cell lines. Specifically, the initial rates of contractile response, defined as the change between the initial tonic reading and first measurement following bradykinin stimulation, were greater in asthmatic lines than normal ones, and this difference in rate was statistically significant (Fig. 4b). Interestingly, despite this initial differential response, which was observed until the third imaging time point, or roughly 12 min (not shown), the total increase over the full course of the experiment was similar between the groups (Fig. 4c). This indicates that while there were clearly differences in the absolute force generation between asthma and normal lines, the differences in their relative responsiveness to agonists may have be dominated by kinetics. Finally, we assessed whether rescue by formoterol was differentially effective among the two groups. Traces of the population medians (Fig. 3c) indicated that a number of cell lines from both groups showed substantial reversal following treatment with formoterol, but both groups

also had cells that responded more asymptotically. Accordingly, when compared collectively, the asthma and normal HASM cell lines manifested similar responsiveness to formoterol. However, a subset of normal-derived cell lines showed substantially greater reversal than any asthma-derived lines (Fig. 4d).

Conventional calcium release assays poorly predict functional contractility in HASM

Using the FLECS workflow, cells may be imaged live or fixed in their contracted state and subsequently phenotypically profiled. Since the cells were confined to micropatterns with known positions and boundaries, a simple algorithm could be used to quantify molecular biomarkers associated with a functional output (for example, contraction) at the single-cell level over a population of cells. We applied this analysis to address the correlation in agonist-induced increases in cytosolic calcium with contraction responses in HASM in a cell-by-cell manner.

Excitation–contraction coupling of HASM requires the highly coordinated activation of calcium mobilization pathways with released calcium from intracellular calcium stores and with calcium influx from the extracellular space. Calcium sensitization activates rho kinase to inhibit myosin light chain phosphatase activity and activate actin polymerization and reorganization pathways, as well as enabling myosin–actin interaction. Some—but not all—of these pathways are calcium dependent and no techniques have previously been demonstrated to distinguish the relative contribution of calcium mobilization with simultaneous measurements of force generation in single cells. Here, by first recording changes in calcium-sensitive dye intensities within HASM arrayed on a FLECS well-plate (Supplementary Video 6) and then monitoring the changes in their respective micropatterns (Fig. 5a–b), we show that the magnitudes of agonist-induced peak calcium and HASM contraction responses are differentially modulated by agonists.

Fig. 5

Simultaneous measurements of calcium release and contractility in patient-derived HASM single cells.

a, Experimental workflow. Adhered cells labelled with Fluo-8 were imaged in their tonic state. Agonists were then added and the calcium-sensitive dye intensity was recorded for 30 s at 100-ms intervals. The same set of micropatterns was then imaged for 25 min at 1-min intervals. Calcium release and contractility traces were extracted from these image series. The black triangle on the individual calcium trace denotes the addition of the agonist. fps, frames per second. **b**, All traces obtained from cells

treated with bradykinin (BK) ($n = 503$ cells). **c**, Population-averaged traces for each agonist. Peak values from the two traces do not correlate, indicating that a high-intensity calcium signal does not necessarily translate to robust contraction. Error bars represent s.e.m. **d**, Correlations between peak calcium release and peak contraction for the same single cells. Histograms displayed horizontally and longitudinally correspond to the isolated contractility and calcium measurements, respectively, and the coloured bar in each distribution identifies the bin containing the median value. While each agonist induced calcium release and contraction to some extent, there were no strong correlations between these measurements.

AQ15

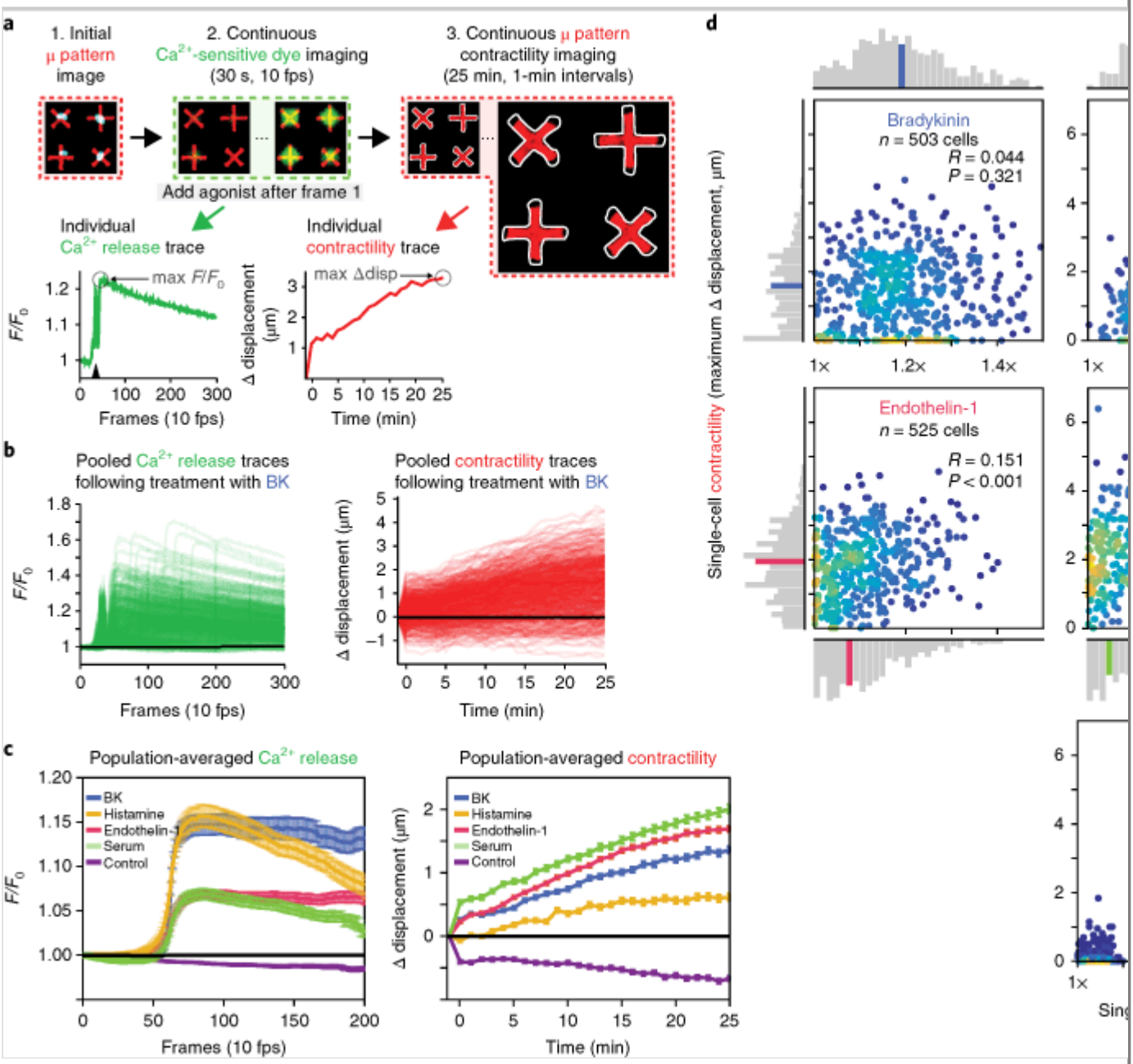

Comparing agonist-induced peak calcium and contraction responses in hundreds of HASM single cells, on average, bradykinin and histamine manifested the greatest calcium responses, whereas the greatest contraction responses were observed with serum and endothelin-1 stimulation (Fig. 5c). Interestingly, at the single-cell level, there were no correlations among peak calcium and maximal contraction for any tested agonist, even when the populations were gated to only include responders (for example, cells exhibiting either >1 μm contraction increases or a >1.1-fold change in calcium dye intensity; Fig. 5d and Supplementary Fig. 6). In fact, some high calcium responders manifested no contraction, while some very weak calcium responders produced substantial contractile responses. Some of these effects may be explained by the activation of receptors differentially coupled to G proteins. For example, histamine activates the histamine 1 receptors coupled to the G_q subunit, which increases phospholipase β, which then activates the canonical inositol 1,4,5-triphosphate pathway. However, it also activates the histamine 2 receptors coupled to the G_s subunit, which increases cyclic adenosine monophosphate and activates protein kinase A, which then antagonizes force generation. The net effect on histamine-induced force generation probably relates to the stoichiometry of the differential receptor activation. Similarly, serum that contains a variety of agonists likely activates a multitude of HASM receptors that have differential effects on calcium mobilization and force generation.

AQ16

Collectively, our data support the hypothesis that agonist-induced peak calcium responses may not correlate with force generation, and that while calcium release assays may generally indicate that contractile pathways have been activated, they have limited usefulness as a quantitative predictor of cellular contractility. These findings suggest that high-throughput screens of force modulators using calcium-sensitive dyes, as have been recently suggested[27] may have significant limitations in terms of specificity and predictivity. Overall, we demonstrate that FLECS allows unique multi-modal studies involving contractility to be performed on single cells in situ, including transient biological events occurring on sub-minute timescales. As with all previous experiments, we achieved relatively large N for all experimental conditions, and all present cells were evaluated automatically by the algorithm. By simultaneously addressing functional and molecular phenotypes in large numbers of cells using automation, FLECS presents new opportunities for discriminating between the modes of actions of biological agonists associated with abnormal contractility diseases.

AQ17

AQ18

Force generation in phagocytosis acts in a digital manner

In innate immunity, mechanical forces direct phagocytosis—the process by which phagocytes internalize and destroy foreign pathogens and clear cellular debris. Operating at the single-cell level, our microtechnology is uniquely suited to evaluate phagocytic forces in individual primary human macrophages—a measurement that has not been previously demonstrated. We achieved this by embedding dansylated bovine serum albumin (BSA) micropatterns into the elastomeric surface and incubating them with anti-dansyl chimeric immunoglobulin G (hIgG). The resultant micropatterned immune complexes reliably promoted a phagocytic response: human monocyte-derived macrophages (hMDMs) rapidly adhered, spread over and contracted the opsonized patterns and maintained the contraction for up to 16 h (Fig. 6a–b and Supplementary Video 7).

Fig. 6

Measuring phagocytic forces generated by individual human macrophages.

a, Representative images of hMDMs on hIgG cross patterns showing a range of phagocytic responses. **b**, Representative image of actin-stained hMDMs spread over circular patterns in an array. High rates of single-cell pattern coverage are achieved. **c**, Phagocytic contraction of (1) ring, (2) cross and (3) filled hIgG circular patterns. The three distributions of single-cell responses were not significantly different. **d**, Opsonin dependence in phagocytic contraction. Vitronectin, fibrinogen, BSA and hIgG were patterned in 50 μm cross shapes on a stiffer, 67:1 base:crosslinker (top) and softer 71:1 (bottom) substrate. HIgG elicited the most contractile response from the largest fraction of macrophages, consistent with the role and urgency of antibody opsonization in immunity. The left *y* axis represents displacement, while the right *y* axis represents applied forces. A typical pattern representing each distribution in the 67:1 case is shown below. In **c** and **d**, '*n*' represents the number of cells in each distribution. **e**, Finite element method modelling of forces exerted by a phagocytosing macrophage. Forces were modelled as boundary loads on a linear elastic material and exerted between all pairs of adjacent terminals of the cross pattern. The shape of the non-displaced pattern is outlined in white and the 5 μm × 10 μm area over which force was applied is shaded. Left: complete geometry comprising a 150 μm × 150 μm elastic material with 90 μm thickness. Middle: top view showing the direction of applied tangential forces, indicated by arrows. Right: cross-sectional view of one-quarter of the geometry at 50% opacity, highlighting the response of the material to the boundary load and indicating the direction of net displacement. Internal columns

of material are depicted only to emphasize the displaced geometry due to applied forces and do not represent real boundaries in the material. The Kruskal–Wallis test for non-parametric data was used to perform statistical analyses on the contractile distributions for the opsonin dependence experiment, with significance defined as $P < 0.05$. For the density dependence experiment, a one-way analysis of variance ruled out any significant differences. Scale bars: 25 μm. NS, not significant.

AQ19

AQ20

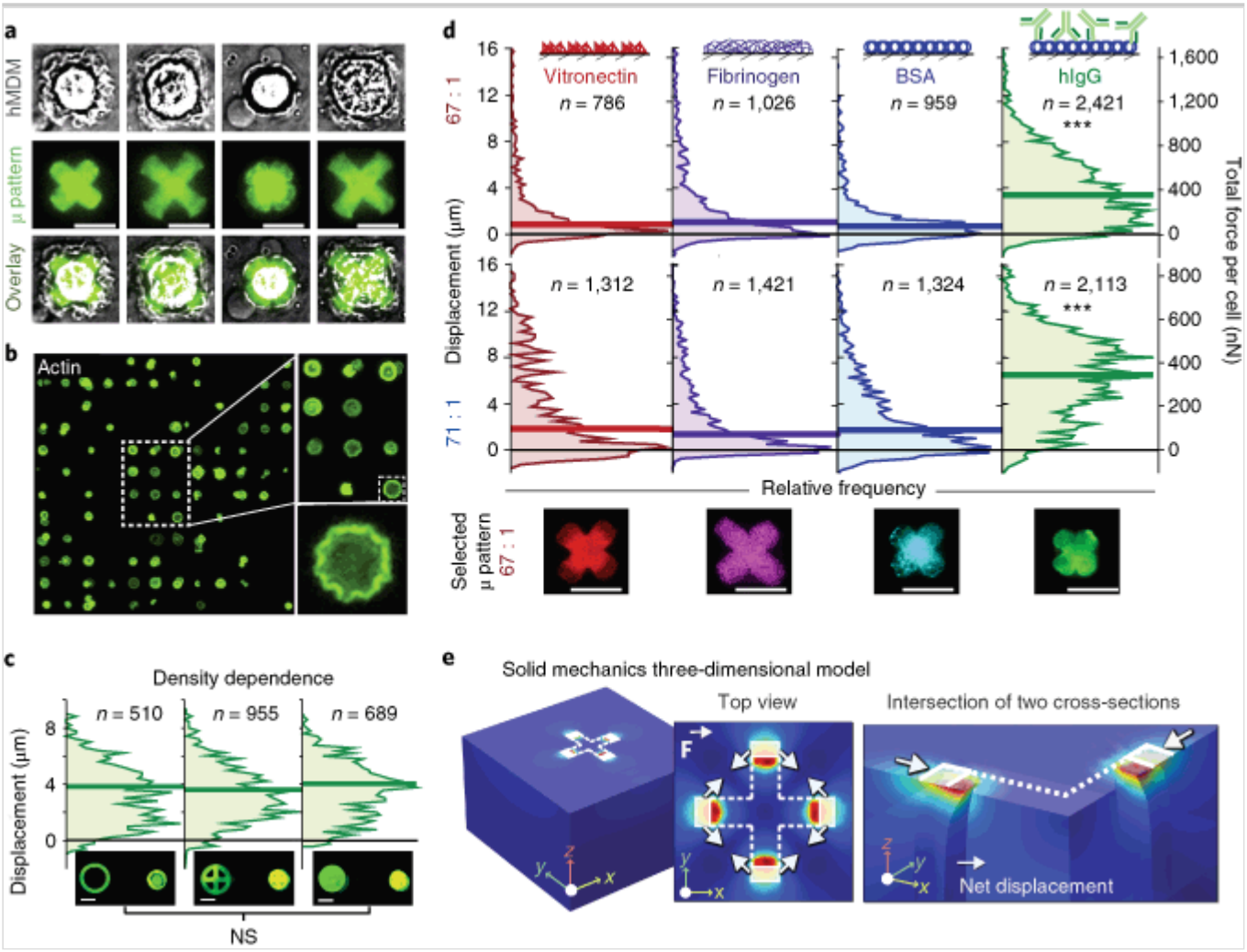

We first investigated the open question of whether the quantity of presented stimulus modulates total phagocytic force. This was done by patterning hIgG into three equi-diametric circular shapes (to control the cell-spread area), but with different interior geometries to vary the quantities of presented antibody. The MDMs spread uniformly over micropatterns of each shape and, surprisingly, produced statistically similar micropattern displacements (Fig. 6c). This result suggests that, as for the triggering of cytokine secretion in T cells[28], the

phagocytic pathway leading to force generation acts in a digital manner, turning 'on' completely at a certain threshold, but not scaling with opsonin quantity.

We expected that forces involved in FcR-mediated phagocytosis would exceed less biologically urgent forces initiated by other adhesive opsonins. To evaluate this, we also examined MDM responses to non-opsonized dansylated BSA, as well as fibrinogen or vitronectin—molecules that support long-term macrophage adhesion but have less understood immunological roles[29, 30]. Micropatterns with hIgG presented with the largest displacements, while micropatterns with fibrinogen, vitronectin and dansylated BSA generally presented with very minute displacements, supporting our hypothesis. However, for each of these three other conditions, there was a small sub-population of MDMs that applied substantial contractile forces comparable to hIgG (Fig. 6d). We suppose this is because a subset of the MDMs, which were initially differentiated from a heterogeneous pool of monocytes[31], had become activated by these molecules through interactions with other (non-FcR) receptors, ultimately converging in downstream signalling pathways leading to phagocytosis—further supporting the notion that phagocytic force generation acts in a digital manner.

AQ21

Macrophages generate hundreds of nanonewtons of force during phagocytosis

Using finite element method solid mechanics modelling based on the micropattern displacements and mechanical properties we measured for the material, we approximated the forces applied onto the micropatterns. We found that MDMs that were engaged in FcR-mediated phagocytosis generated median forces of ~350 nN while a number of outlier cells were capable of forces as large as 1 μN (Fig. 6d–e). Median forces generated by MDMs on the other opsonins were significantly less, never exceeding 100 nN. Forces in the 10^{-7} N range have previously been reported for other human cells, including MSCs, human umbilical vein endothelial cells[22] and keratinocytes[32]. Phagocytic forces in this range should be expected as the adhesive strengths of certain bacteria were also found to approach the μN range[33]. It is also interesting to note that the macrophages generated similar levels of force on both substrates despite differences in their stiffnesses, since a previous study reported a correlation between forces in migrating macrophages and substrate stiffness[34]. The lack of such a relationship here is probably due to the difference in behaviours being analysed. Specifically, while there may be physiological reasons for more rapid migration on stiffer surfaces, there does not appear to be a benefit to modulating the phagocytic force if the objective is rapid

clearance of a foreign entity. Moreover, it is possible that the response is only linear on the small range of stiffnesses we tested (4–8 kPa), and that it may behave differently over a larger range. Overall, this analysis represents the first direct quantification of the contractile forces involved in the closure of the phagocytic cup.

Subclasses of IgG stimulate similar phagocytic force generation

A recent study reported minor differences in the ability of different IgG subclasses to stimulate the phagocytic uptake of *Salmonella* bacterial cells by a monocytic cell line[35]. We asked whether these differences were triggered at the force-generation level. Using a humanized panel of the four subclasses of IgG antibodies, we found that all subclasses induced significant and comparable increases in phagocytic force over the non-opsonized controls. We observed a similar result for another phagocyte—matched immature monocyte-derived dendritic cells derived from the same patient (Supplementary Fig. 7). It is not entirely surprising that MDMs and monocyte-derived dendritic cells produced similar forces since both are professional phagocytes with the same general targets; for example, bacteria, parasites and debris. However, these results suggest that if phagocytic uptake efficiency does indeed differ among the subclasses, it is not a result of differences in force generation.

Pharmacological inhibition of actin polymerization but not of phagosome acidification reduces the phagocytic force

Actin polymerization has long been known to be required for phagocytosis, with target uptake assays showing that actin inhibitors greatly reduce phagocytic efficiency, particularly with Fc-opsonized targets[36]. Given its role in phagosomal closure, it is logical that inhibition of polymerization would reduce the phagocytic force. Following closure, the internal phagosomal pH progressively decreases, enhancing its microbicidal activity[37]. It remains unknown whether there is feedback between phagosome maturation and the sustained maintenance of a phagocytic force.

We used FLECS to confirm the direct role of actin polymerization in phagocytic force and also to determine whether disruption of phagosomal acidification (a late-stage event) feeds back into the control of the earlier mechanical stages of phagocytosis. We treated MDMs with cytochalasin D or chloroquine at three doses to block actin polymerization or phagosomal acidification, respectively. MDMs were either seeded directly into drug-containing medium or incubated with the drug

after achieving steady-state phagocytic contraction on hIgG 'X' patterns. As expected, incubation with cytochalasin D at all the tested doses substantially decreased the measured phagocytic contraction, while pre-treatment completely prevented any measureable contraction, confirming the requirement of actin polymerization in phagocytic force generation (Fig. 7a–d). Treatment with chloroquine had no effect on the mechanical output of the macrophages, indicating that the early-stage mechanical encapsulation and chemical maturation involved in phagocytic clearance are uncoupled in both the long and short term.

Fig. 7

Effects of chloroquine, cytochalasin D and CAL-101 on hMDM contractile force.

a, Contraction distributions of hMDMs engaging IgG-opsonized micropatterns pre-treated with DMSO or three doses of each drug. **b**, Contraction distributions of hMDMs engaging IgG-opsonized micropatterns incubated with DMSO or three doses of each drug for 15 min after reaching steady-state contraction. In **a** and **b**, the data are pooled from four technical replicates and '*n*' represents the number of cells in each distribution. A bimodal distribution was observed reflecting an 'active' phagocytosing population (red curve) and a weakly adhered, inactive population (blue curve). A mixed Gaussian distribution is fitted to each plot to obtain information about the active populations, which is used for quantification. **c**,**d**, Median contraction levels of the active populations in **a** and **b**, respectively. Bars represent the mean of four replicates and error bars represent the s.e.m. of no treatment and treatment with DMSO control. Measurements were compared using analyses of variance followed by two-tailed Bonferoni-corrected *t*-tests. NS, not significant.

AQ22

AQ23

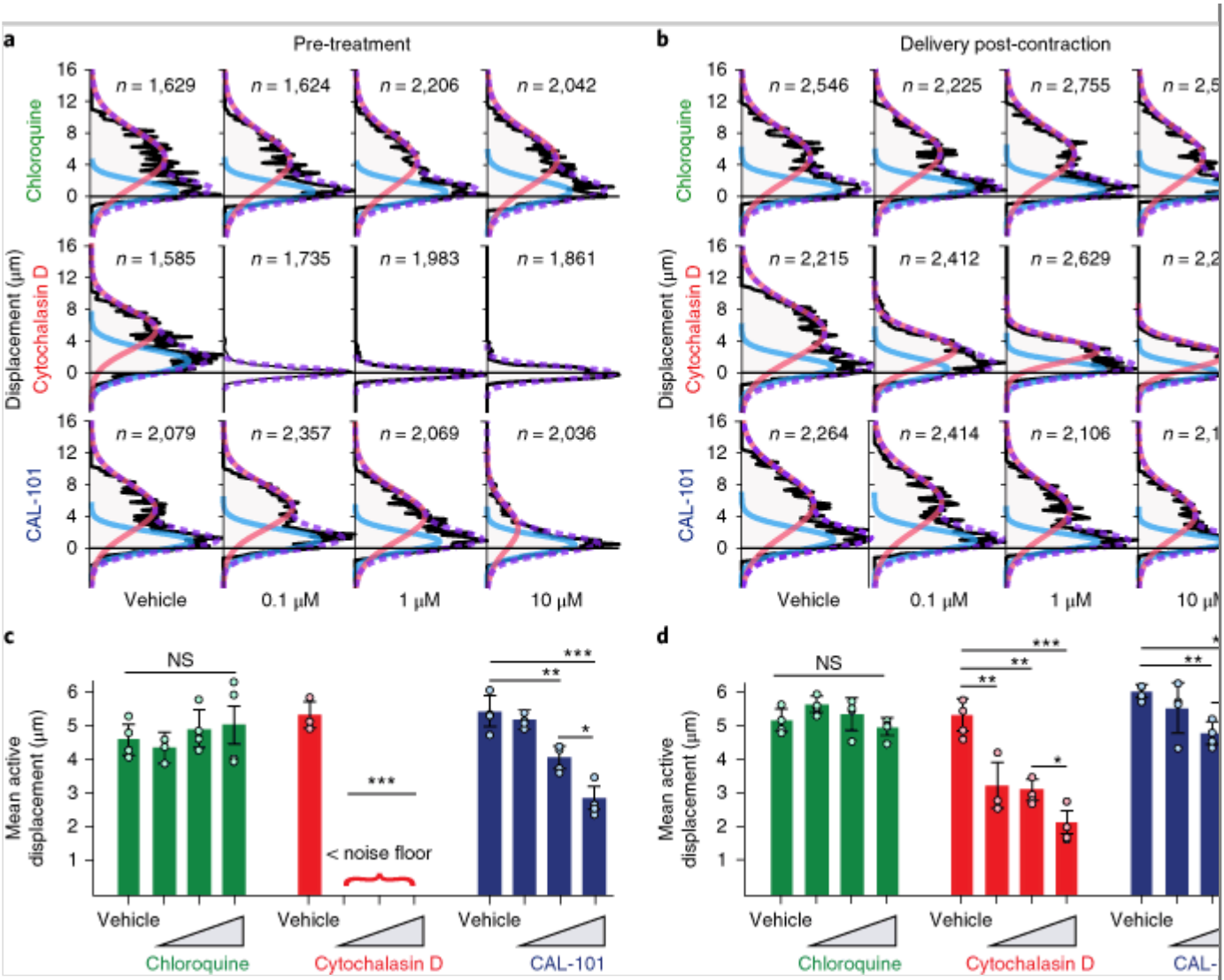

PI3K inhibition reduces the forces generated during FcR-mediated phagocytosis

Finally, we investigated the role of a specific phosphatidylinositide 3-kinase (PI3K) isoform, p110δ, in phagocytic force. Among other roles, PI3Ks regulate phagocytosis by driving re-arrangement of actin in phagosome formation[38, 39]. Class 1A PI3Ks—the p110α, p110β and p110δ isoforms—positively regulate the small G protein Rac1 (ref. [40]), which coordinates actin organization and is required for FcR-mediated phagocytosis[41, 42]. Of these, the p110δ isoform has also been shown to selectively reduce phosphorylation of Akt, which is an upstream effector of FcR-mediated phagocytosis[43] and negatively regulate the PI3K antagonist PTEN in murine macrophages[44]. To test whether PI3Kδ inhibition attenuates the forces generated in FcR-mediated phagocytosis, we subjected hMDMs contracting our hIgG micropatterns to three steps of tenfold dilutions of the selective p110δ inhibitor CAL-101.

We found that at the effective dose of 1 μM, compared with the vehicle control, CAL-101 produced statistically significant relaxations in micropatterns occupied by the active population of macrophages, and at 10 μM the effect was even more pronounced, indicating a dose-dependent response (Fig. 6a–d). Although pre-treatment with CAL-101 produced a more robust relaxation at all doses, the post-contraction incubation revealed the rapid onset of this effect (which became noticeable within 15 min of compound addition) and corroborated the requirement of PI3K activity for sustained force generation. This observation shows that PI3K plays a direct role in phagocytic force generation. The partial suppression of baseline phagocytic force at the effective dose is consistent with reports that PI3K inhibition blocks phagocytosis of large targets but not smaller ones[38]. It is also possible that the redundant functions of the other class 1A PI3Ks helped to mitigate the relaxing effects of this selective p110δ inhibition. This observation is important to consider in terms of the potential immunosuppresive side effects of CAL-101, which is currently in phase III clinical trials for the treatment of chronic lymphocytic leukaemia (Clinical Trials Identifier NCT01539291).

Discussion

The FLECS system combines advances in the preparation of bio-functionalization of soft materials with compatibility with automation workflows to enable high-throughput and multi-modal analysis of large populations of a variety of contractile cells. The core material allows for independently tunable stiffness, pattern shape and molecular composition, enabling it to be tailored to a broad range of cell types and their functions. The seamless integration with well-plate formats enables direct use with screening robotics and high-content imagers, as well as simple adoption by end users. As such, this system has the potential to address both research and industrial applications.

For example, the functionalization of our sensors with immunological molecules enables the study of phagocytosis of large targets. Traditional phagocytosis assays are endpoint measurements that look at the total engulfment by phagocytes of exclusively smaller targets. In contrast, our larger, surface-bound targets are a good model for phagocytosis of tissue-like structures such as biofilms or tumour cells embedded in tissue. In addition to quantifying phagocytic force, this method could help determine which factors can lead to improved immune cell disruption of such pathogenic tissue-like structures. By simply altering the surface functionalization, evaluations of forces by many other cell types, including SMCs and cardiomyocytes (Supplementary Fig. 8 and Supplementary Videos 8–10) also become possible.

The compatibility of the FLECS system with automation enables precise execution of multi-parametric studies of large quantities of different cells. We were able to simultaneously evaluate tone, responsiveness to an agonist and subsequent responsiveness to a countering antagonist for >1,000 cells from each of 12 patient-derived cell lines at once using a single FLECS well-plate. The overall yield of ~31,000 cells on the plate, of which ~24,000 were robust responders and used for analysis, exceeds previously reported throughputs for individual contractility experiments (which we define as comprising a single cell-seeding session and single execution of analysis software) by 100-fold. By analysing this many cells simultaneously, we were able to definitively report that asthma HASM innately produces larger forces than non-asthma HASM.

Although we observed clear differences between multi-potent and differentiated cells, the differences between osteocytes and adipocytes were less apparent, despite past reports showing such differences using micropost arrays[22]. Whether this discrepancy is a result of the fundamentally different physical environments presented to the cells (continuous planar versus discretized deflectable pillars), different culture conditions (in situ versus in vitro) or resolution limitations is unclear. Therefore, it is important to note that each of the three major laboratory methods for measuring cellular force offer unique strengths and limitations, and a given biological problem may be better suited to one method over another. These are summarized in Table 1 and discussed below.

Table 1

Comparison between FLECS and existing methodologies for measuring cellular force

Method	TFM	Micropost arrays	FLECS
Fabrication	Uses particle mixing with ultraviolet-cured gels; micro-contact printing used for uniform single-cell measurements	Uses device delamination from moulds and functionalization via stamping with protein; micro-contact printing used for uniform single-cell measurements	Uses micro-contact printing on a sacrificial layer; inherently single-cell
Other requirements	Automated cell detection uses fluorescent tagging of cells	Oil-/water-immersion high magnification objectives used[22][,54,55]	Uses nuclear stain

Method	TFM	Micropost arrays	FLECS
Image analysis	User typically defines region of interest by manually tracing cells[56, 57, 58]; automated cell detection possible with additional cell-labelling procedures[59]	User manually locates cells and identifies ‘attached’ and ‘unattached’ posts[13, 54, 60]; automated cell detection possible with additional cell-labelling procedures[22]	Micropatterns detected via template-matching algorithm; nuclei counting and micropattern measurements performed using an algorithm
Spatial resolution	Sub-cellular	Sub-cellular	Whole-cell
Time-course	Cell migration tracking used if cell not patterned; cells removed following final time point to obtain reference	Cell migration tracking used if cell not patterned; adhesion/de-adhesion to microposts is tracked	Cell locations preserved; no additional action required
Used in automation workflow?	Bulk-averaged: yes[12]; single-cell: not reported	Not reported	Yes (demonstrated herein)
Data throughput/experiment	Typical: 10–50 cells[11, 14, 19, 20, 61]; maximum reported: >1,000 cells (not single-cell)[12]; ~100 cells (single-cell) [62]	Typical: ~10–25 cells[15, 54, 55, 60]; maximum reported: ~100 cells[22] (all single-cell)	Typical: >1,000 cells; maximum reported: >30,000 cells (all single-cell)
Top application areas explored	Bulk-averaged traction moment measurements[12]; mapping complex, sub-cellular traction forces in individual cells[63]; force measurement during cell migration[11, 34]; correlating traction force with morphology and focal adhesions[20] [,21,64]	Resolving minute sub-cellular differences in related cell types[22]; T cell force generation[65]; decoupling stiffness from porosity; accurate calculation of absolute force (per micropost)	Large-count single-cell measurements; rapid time-course for large populations; identification of outliers; co-measurements of phenotypic makers; high-throughput screening

TFM and micropost array methods offer superior spatial resolution that is able to assign force vectors to specific focal adhesions and measure very subtle forces in small cells like T cells. Advanced TFM techniques are now able to map complex sub-cellular forces in three-dimensional polymer and gel networks. In general, both methods should remain the standard for addressing specific biological questions relating to sub-cellular force generation by small numbers of cells. However, this resolution comes at the cost of simplicity and throughput, as these methods typically require high magnification imaging and manual user input during analysis workflows. Thus, as shown in Table 1, the experimental data throughputs have generally been limited to 10–50 cells.

In comparison, FLECS yields a larger quantity of single-cell data per experiment than the older methods. Instead of manually tracing or fixing and staining cells (which may alter the observable contractile phenotype substantially), FLECS analysis locates live cells based on nuclear staining co-localized to micropattern sites using automated template-matching and binary segmentation algorithms. Thus, no user input is required and all imaged cells are analysed, thereby removing the potential for selection bias. Furthermore, by taking whole-cell rather than sub-cellular force measurements, FLECS is able to extract quantitative data from much larger fields of view with smaller pixel sizes (for example, data presented in Figs. 3 and 4 were extracted from images taken with 1.61 $\mu m\ px^{-1}$ sizes) relative to the older methods. Finally, as discussed at length, FLECS is the only methodology demonstrated to integrate into a high-throughput phenotypic screening configuration that maintains single-cell resolution. These features enable FLECS to achieve the described 100-fold improvements in throughput.

All three methods are suitable for performing time-course measurements of cellular force. However, in addition to throughput limitations, unconstrained cells in the native TFM and micropost systems migrate and require precise monitoring, adding a layer of complexity to the measurements. This problem can be overcome by incorporating micro-contact printing steps to restrict cell motion, although this may present additional fabrication difficulties. With FLECS, cells are inherently restricted to micropatterns and do not migrate. For the same reason, FLECS inherently provides single-cell resolution, which allowed us to longitudinally track cellular contractility following calcium imaging in the same single cells to discover that peak measurements in these two modes are not well correlated despite calcium flux being commonly used as a direct upstream indicator, as well as to select for responding cells from both HASM and macrophage populations to cleanly resolve agonist effects.

As a result of these unique advantages, FLECS has the potential to become the leading technology for phenotypic drug discovery pertaining to conditions involving aberrant cellular force generation. Compared with target-based screening, phenotypic screening has produced more first-in-class medicines due to its naturally unbiased identification of the molecular mechanism of action[45].

Methods

Preparation of patterned ultra-soft substrates

The wafer-scale process is shown in Supplementary Fig. 9 and has been described in detail previously[46]. Briefly, a 20% dextran solution (70 kDa; Sigma–Aldrich) in deionized water was spin-coated onto plasma-activated silicon wafers and baked until dehydration to yield dextran substrates. Chrome photomasks containing arrays of micropatterns were designed using L-Edit software, fabricated off-site and used to pattern SPR 220 photoresist on separate silicon wafers. Polydimethylsiloxane (PDMS; Sylgard 184) at 10:1 base-to-crosslinker ratio was cast onto the patterned wafer, cross-linked and demoulded yielding stamps with positive pattern features. Adhesive biomolecule (for example, extracellular matrix protein) solution was added to the stamp surface, incubated for 1 h and air-dried immediately before stamping. The stamped adhesive molecule or a co-stamped molecule was conjugated with a fluorescent moiety. Dextran substrates were activated with a brief plasma treatment and stamped with the biomolecule-adsorbed PDMS stamps for 5 min. Ultra-soft PDMS mixture (55:1 to 71:1) was spin-coated (1,200 rpm; 20 s) over the stamped dextran-coated silicon and cured (24 h at room temperature followed by 7 days at 65 °C). Once cured, the substrate could be stored stably at room temperature for more than nine months.

AQ24

AQ25

AQ26

Releasing substrates and seeding with cells

To begin an experiment, the substrate was mounted onto cover glass (where the PDMS layer was in contact with the cover glass) and placed into saline solution to release the soluble dextran layer and yield a glass-backed elastomeric thin-film with embedded proteins. This substrate could be fabricated as large as a well-plate footprint. Following fabrication, the sample was sterilized by washes in strong base followed by washes in sterile deionized water. Non-patterned regions were blocked in a 0.5% solution of Pluronics F-127 (45 min at room temperature) and cells of

interest were seeded. For live imaging experiments, Hoechst 33342 nuclear stain was added to the culture medium (1 μg ml^{-1} final concentration). If cells were to be fixed, the nucleus was stained after fixation. The sample was washed to remove non-adhered cells after 2 h. At the conclusion of the experiment, the sample was either left unfixed or fixed in 4% paraformaldehyde solution at room temperature for 1 h, mounted using 4',6-diamidino-2-phenylindole-infused mounting medium and imaged.

Imaging and image analysis

In our experiments, fluorescent patterns (green or red channel) and cell nuclei (blue channel) were imaged at 10× magnification with a Nikon fluorescence microscope in fixed-sample experiments, or with the ImageXpress Micro XL High-Content Imaging System fluorescence microscope with 10× magnification for end-point experiments or 4× magnification for time-course experiments. Image processing was performed using MATLAB.

A separate algorithm was developed for analysing each pattern type. For experiments using cross (‘X’) patterns, a template was used to locate all patterns in all frames. The mean distance between the centre and each terminal of each pattern comprised a data point. For experiments using circular patterns, the native MATLAB function *imfindcircles()* was used to identify all circular shapes in each frame and measure their radii. The presence or absence of a stained nucleus at the corresponding *xy* location of the nuclear image determined whether a given pattern was used for the control or experimental data or was rejected as having multiple cells (Supplementary Fig. 2a). All experimental data measurements were zeroed to the median of the measurements of control case patterns yielding net displacement histogram plots. Raw measurements were also saved in a .mat format. M-Files containing the algorithms for calculating ‘X’ micropattern displacements and measuring dye intensity within adhered cells are supplied in the Supplementary Information.

During processing, a file containing (1) an image of each cross pattern marked at the computed centre and vertices, or an image of each circular pattern overlaid with the circle fitted by the *imfindcircles()* function, alongside (2) an image of the corresponding nuclear signal labelled with the computed cell count, was created and saved for each pattern–nuclear-signal pair for later viewing and quality control (Supplementary Fig. 2b).

AQ27

Study on mesenchymal stem cells

Cell culture and differentiation

Human MSCs derived from bone marrow or adipose tissue (StemPro; Thermo Fisher Scientific) were maintained in MesenPRO RS Medium. Differentiation was induced by 14-day culture in adipogenic (StemPro Adipogenesis Differentiation Kit) or osteogenic (StemPro Osteogenesis Differentiation Kit) inductive medium as described in the manufacturer's manual. Trypsin-EDTA (0.05%) was used to re-suspend cells at the start of the experiment. Seeding and culturing on FLECS substrates was done in Dulbecco's modified Eagle's medium (DMEM; Invitrogen) supplemented with 10% MSC-qualified foetal bovine serum (FBS), 100 units ml^{-1} penicillin and 100 μg ml^{-1} streptomycin. Early passages (<7) of hMSCs were used in all experiments.

Substrate parameters

Cross-shaped patterns (70 μm diagonal; 10 μm bar thickness) spaced at 100 μm centre-to-centre vertical and horizontal distances were used for this experiment. Substrates were prepared by adsorbing 0.5 ml of 30 μg ml^{-1} fibronectin and 30 μg ml^{-1} Alexa-Fluor-488-conjugated fibrinogen solution to each of six 22 mm × 22 mm stamps for 45 min before stamping dextran-coated wafers. PDMS was mixed at a 55:1 base-to-crosslinker ratio.

Experimental procedure

Substrates were housed in six-well plates during the experiment. Cells were seeded by pipetting cell suspensions directly over the substrates. After 1 h, non-adhered cells were washed away. Cells were fixed with warmed 4% paraformaldehyde, and the substrates were mounted onto glass slides using 4',6-diamidino-2-phenylindole-infused mounting medium (P-36931; Thermo Fisher Scientific) 8 h after seeding and later imaged.

Actin staining

Following fixation but before mounting, a subset of all MSC samples was permeabilized with 0.25% Triton X-100 (Sigma–Aldrich) for 10 min and incubated with 1:500 Alexa Fluor 568 Phalloidin (A12380; Thermo Fisher Scientific) in phosphate buffered saline (PBS) for 20 min at room temperature.

Study on tonic traction forces supplied by primary human SMCs

Cell culture

Cryopreserved human primary bronchial, uterine and aortic SMCs were purchased from PromoCell. The cells were maintained in complete Smooth Muscle Cell Medium (PromoCell) supplemented with 100 units ml^{-1} penicillin and 100 μg ml^{-1} streptomycin. Trypsin-EDTA (0.05%) was used to re-suspend cells at the start of the experiment. Seeding and culturing on FLECS substrate was also done in Complete SMC 2 Medium (PromoCell). An end-point measurement was obtained from one well for each SMC source 8 h after seeding.

Blebbistatin titration

Blebbistatin (Sigma–Aldrich) was dissolved in DMSO to achieve working concentrations using 10 steps of twofold dilutions beginning with 25 μM. HASM cells were seeded 24 h before treatment with blebbistatin. On the day of the experiment, cells were stained with Hoechst, washed, treated with blebbistatin (1% DMSO final concentration), incubated for 30 min and imaged live using the ImageXPress Micro XL High-Content Imaging System.

Statistical analysis

Each concentration of blebbistatin was tested in four technical replicates. The median contraction at each concentration was normalized by vehicle-treated contraction. GraphPad Prism 6 graphing software was used to fit a sigmoid curve to the dose-response data and calculate the half-maximal inhibitory concentration.

AQ28

Evaluation of asthma and non-asthma patient-derived HASM

Isolation and culture of HASM

All lines of HASM cells were derived from tracheas obtained from the National Disease Research Interchange (Philadelphia, PA, USA) and the International Institute for the Advancement of Medicine (Edison, NJ, USA). HASM cell culture was performed as described previously[47, 48, 49]. Briefly, the cells were cultured in Ham's Fâ€ 12 medium supplemented with 10% FBS, 100 U ml^{-1} penicillin, 0.1 mg ml^{-1} streptomycin and 2.5 mg ml^{-1} amphotericin B, and this medium was replaced every 72 h. HASM cell passages 1–6 were used for all experiments because these cells retain the expression of native contractile protein, as demonstrated by immunocytochemical staining for smooth muscle actin and myosin[47]. The HASM cells were derived from donors with fatal asthma or donors

who were age and gender matched without asthma, as shown in Supplementary Table 1.

The 12 distinct patient cell lines were seeded into 8 wells column-by-column, alternating between non-asthmatic and asthmatic lines, in each of 3 FLECS well-plates at approximately 5,000 cells per well and allowed to adhere for 2 h, at which point serum was removed for 24 h before pro-contractile agonists were added.

AQ29

Basal tone

The three plates were imaged on an ImageXpress High-Content imager with environmental controls before any stimulation to get a basal measurement for contraction.

Responsiveness to bradykinin and formoterol

Immediately after acquiring baseline images, one of the three well-plates (selected at random) was used to perform pharmacological studies, and a multi-drop instrument (BioTek) was used to deliver bradykinin (Sigma–Aldrich) to all 96 wells at a final concentration of 10 μM. The plate was replaced on the imager and each well was imaged for 16 min at 4-min intervals. Following the last imaging time point, the plate was removed and the multi-drop was used to deliver 50 μM formoterol (Sigma–Aldrich) to every odd row or 1% DMSO in serum-free medium to every even row. The plate was again replaced and imaged an addition six time points. Analysis software was used to track the contractile behaviour of each of the 250–450 cells adhered within each well (>31,000 cells in total) over the course of the experiment, and those cells exhibiting a positive contraction between the initial and fourth time point (after 16 min of bradykinin stimulation but before formoterol or vehicle) were selected for further analysis—approximately 24,000 cells.

Simultaneous measurements of calcium release and contractility in HASM single cells

Experimental

HASM cells derived from a single healthy patient were seeded into a FLECS well-plate as described above and serum-starved for 24 h. Before imaging, cells were incubated with 4 μM Fluo-8 (Abcam) and 1 μg ml^{-1} Hoechst 33342 for 1 h and then washed with fresh serum-free medium. To start the experiment, 20 wells were imaged using 4× magnification on the ImageXpress to get a baseline reading. The plate was immediately transported to a table-top manual fluorescence microscope

(Nikon) where serum-free medium, 20% FBS (Thermo Fisher Scientific), 10 μM bradykinin, 100 nM endothelin-1 (Sigma–Aldrich) or 10 μM histamine (Sigma–Aldrich) was added to four wells each, one-by-one, and the calcium dye intensity was imaged for 30 s at 100-ms intervals (see Supplementary Video 6). After the imaging was complete for the final well, the plate was transported back to the high-content imager to acquire images of the micropatterns for 25 min at 1-min intervals.

Analysis

Image series of the micropatterns and image series of the calcium signal, which were acquired on separate microscopes, were registered using corresponding images of stained cell nuclei taken through both microscopes, which produced a unique intensity signature at each site allowing simple registration in ImageJ. Single-cell contraction was assessed as usual. Micropatterns in the images taken at the initial time point were used to define regions of interest for each cell within which calcium dye intensity was calculated for every frame and normalized to initial intensity. In the case of 20% serum, addition generated significant sustained auto-fluorescence so the authors manually adjusted the reference intensity for those wells as it was clear from the traces when the calcium peaked relative to the addition of serum. The other agonist did not produce a sustained auto-fluorescence. Both the calcium release and contractility traces were pooled and averaged to generate the mean traces shown in Fig. 4c. The initial calcium peaks were used to register all calcium traces before averaging. The peak values obtained from each single-cell contractility and calcium trace were also displayed in a scatter plot to generate Fig. 4d.

AQ30

Phagocyte experiments

Macrophage differentiation

Human peripheral blood monocytes were isolated from blood taken from consenting healthy adult donors using density gradient centrifugation with Histopaque-1077 solution (Sigma–Aldrich) according to University of California, Los Angeles Institutional Review Board protocol 14-000522. Collected mononuclear cells were washed in saline, re-suspended in unsupplemented RPMI 1640 Medium (Life Technologies) and allowed to adhere to the well surfaces within polystyrene 6-well plates for 2 h. The wells were then washed to remove contaminating lymphocytes and refilled with warm RPMI 1640 Medium supplemented with 20% heat-inactivated foetal calf serum (FCS), 20 ng ml^{-1} M-CSF (Life Technologies), 100 units ml^{-1} penicillin and 100 μg ml^{-1} streptomycin.

Monocytes were allowed to differentiate into macrophages (hMDM) for seven days. All macrophages were used within this period as the phagocytic force was significantly reduced in macrophages aged >14 days and completely suppressed in macrophages aged 21 days (Supplementary Fig. 10). To begin an experiment, macrophages were dissociated from the well-plates by incubation in StemPro Accutase (Life Technologies) for 30 min at 37 °C, followed by vigorous pipetting up and down to complete dissociation. Macrophages were re-suspended in RPMI 1640 Medium supplemented with 10% heat-inactivated FCS, 100 units ml^{-1} penicillin and 100 μg ml^{-1} streptomycin before seeding onto the FLECS chips. Macrophages were imaged live without fixing in all experiments and Hoechst 33342 (1 μg ml^{-1}) was used to stain the cell nuclei.

Dendritic cell differentiation

Dendritic cells were prepared in the same manner as macrophages, but using differentiation medium containing 100 ng ml^{-1} granulocyte-macrophage colony-stimulating factor and 50 ng ml^{-1} interleukin 4 instead of M-CSF.

AQ31

Patterning antibodies

To pattern the IgG antibodies, a 45 μg ml^{-1} dansyl-conjugated BSA and 45 μg ml^{-1} Alexa-Fluor-488-conjugated BSA solution were adsorbed to a stamp and stamped onto a dextran-coated wafer. After the substrates were coated with PDMS, cured, released and blocked with Pluronic F-127, but before the macrophages were seeded, approximately 50 μl per 400 mm^2 of 25 μg ml^{-1} solution of human–mouse chimeric anti-dansyl IgG antibodies was spread over each patterned substrate and incubated for 3 h at room temperature. Excess antibody was then washed with saline. The human–mouse chimeric antibodies were developed by ref. [50].

Density dependence experiment

Circular patterns with 54 μm diameters but with various degrees of filling were patterned with IgG as described above. Specifically, the following were patterned: (1) a ring pattern with 10 μm thickness (inner diameter subtracted from the outer diameter), (2) the same ring pattern encircling a symmetric cross shape with a 10 μm bar thickness and (3) a solid circle. PDMS was mixed at a 65:1 base-to-crosslinker ratio. Macrophages were imaged 6 h after seeding.

Opsonin dependence experiment

Human recombinant vitronectin (Advanced BioMatrix), fibrinogen (Life Technologies) and BSA (Life Technologies) conjugated with Alexa Fluor 488 and hIgG (as described above) were patterned in cross shapes (50 μm diagonal and 20 μm bar thickness). The total quantities of each ligand were set to be approximately uniform by modulating the concentrations of the adsorbing ligands and confirmed by measuring the fluorescence intensities of the resulting transferred patterns (Supplementary Table 2). Macrophages were dissociated as described, seeded and imaged live 6 h later. PDMS was mixed at both 67:1 and 71:1 base-to-crosslinker ratios.

AQ32

Patterning equal quantities of different opsonins

Testing the phagocytic force response of hMDMs as a function of the opsonin type required patterning of three different ligands: vitronectin, fibrinogen and dansyl-BSA (hIgG was not patterned, but rather used to bind the dansyl-BSA in which the conjugated dansyl group served as the binding site for the IgG antibodies). To decouple the potential effects of differential opsonin quantities from the opsonin type, we set out to equalize the molar quantities of each opsonin on our substrates. To accomplish this, each opsonin was labelled with the same fluorophore (Alexa Fluor 488), and the respective degree of labelling (DOL) along with the fluorescent intensities of the patterns as a function of the solution concentration (used in the adsorption step) were used to achieve the same final surface densities. For each fluorescence intensity measurement, 10× magnification and 2 s exposure times were used.

Fibrinogen

Alexa-Fluor-488-conjugated fibrinogen was purchased from Life Technologies (catalogue number F13191; lot number: 1636855) with a DOL of 6. This was the same ligand as was used for the hMSC and dose-response experiments and was adsorbed to the PDMS stamps for 45 min before being stamped onto the dextran-coated wafers for 5 min. Three concentrations (30, 20 and 10 μg ml^{-1}) were tested to create a concentration-versus-fluorescence-intensity curve.

BSA

Alexa-Fluor-488-conjugated BSA was purchased from Life Technologies (catalogue number A13100; lot number 1348652) with a DOL of 7. Alexa-Fluor-488-conjugated BSA was co-patterned with dansyl-BSA since Alexa-Fluor-488-conjugated BSA was used for fluorescently visualizing the pattern while dansyl-

BSA contained the epitope (dansyl) targeted by our human–mouse chimeric antibody. Thus, the two BSA molecules were patterned in equal quantities at three concentrations (60, 30 and 20 μg ml^{-1} each) to create a concentration-versus-fluorescence-intensity curve. In addition to the general procedure, the PDMS stamps were plasma treated before adsorption to promote wetting and, during stamping, the stamps were kept in contact with the dextran-coated wafers under weight for 20 min rather than 5 min.

HIgG

BSA patterns were prepared as described with the addition of hIgG (50 μl of 25 μg ml^{-1} solution per 400 mm^2) after the release, sterilization and blocking steps.

Vitronectin

Human recombinant vitronectin was purchased from Advanced BioMatrix (catalogue number 5052) and conjugated with Alexa Fluor 488 in house using Alexa Fluor 488 carboxylic acid and succinimidyl ester (Life Technologies) at a 8:1 fluorophore-to-protein molar ratio in PBS (4 h at 4 C). Following the reaction, the vitronectin solution was dialysed against PBS for 48 h with PBS changes every 12 h to remove unreacted dye. The DOL for the vitronectin–Alexa Fluor 568 conjugate was calculated to be 6.25 using absorbance readings taken at 494 and 280 nm, as prescribed in the manufacturer's manual provided with the conjugation kit (Life Technologies), and using 1.02 ml mg^{-1} cm^{-1} as the extinction coefficient for vitronectin[51]. Three concentrations (40, 30 and 20 μg ml^{-1}) were tested to create a concentration-versus-fluorescence-intensity curve. As with BSA, the stamps were plasma treated before adsorption and were kept in contact with the dextran-coated wafers under weight for 20 min.

BSA

BSA was found to saturate in fluorescence intensity when 30 μg ml^{-1} and higher concentrations were used for each BSA conjugate. However, concentrations of 60 μg ml^{-1} produced the most consistent transfers so this concentration was chosen for BSA. This maximum BSA intensity was normalized by the DOL for BSA and adjusted by a factor of two to account for the equal part of non-fluorescent BSA (dansyl-BSA). Referencing this target-normalized intensity (termed the 'relative surface molarity coefficient'), along with the concentration-versus-fluorescence-intensity curves constructed for vitronectin and fibrinogen and their DOLs, we predicted the adequate concentrations to be 30 μg ml^{-1} and 10 μg ml^{-1} for vitronectin and fibrinogen, respectively.

AQ33

Approximation of phagocytic forces

Substrate stiffness measurement

Cylindrical PDMS samples (67:1 and 71:1) were placed onto an Instron tensile tester (model 5564) with a 2.5 N load cell, and compressive testing of the sample was performed at a strain rate of 1 mm min^{-1} for a total indentation of 1.5 mm. The data were used to generate load-displacement curves. The slope of the linear portion of the curve, cross-sectional area of the indentation tip and PDMS sample heights were used to calculate stiffness. Three samples of each stiffness were test after one and three weeks of curing (Supplementary Fig. 11). The results showed no significant stiffening after one week, indicating that the polymer was fully cured at one week and these unchanging stiffness values could be used for modelling cellular traction forces. The mean calculated stiffnesses were used in force approximations.

Finite element method modelling

To approximate the forces applied by phagocytosing macrophages on the ultra-soft substrates, the FLECS ‘X’ pattern was simulated using the finite element model software COMSOL. Specifically, a single cross-shaped pattern corresponding to the experimental patterns (50 μm diagonal and 10 μm bar thickness) was simulated. We modelled the ultra-soft substrates as linear elastic materials with Young’s moduli of 4,000 and 7,900 Pa (corresponding to 71:1 and 67:1 PDMS ratios, respectively), a density of 970 kg m^{-3}, a Poisson’s ratio of 0.49999 and the forces exerted by macrophages as boundary loads directed tangentially between all pairs of adjacent terminals of the ‘X’ pattern. The substrate was modelled as a 150 μm by 150 μm film with a thickness of 90 μm and was discretized into tetrahedral mesh elements. A 90 μm thickness was selected to minimize the computational intensity associated with higher degrees of freedom, as thicknesses greater than 70 μm did not yield significant changes in the pattern deflection for a given applied force (empirically, substrates were determined to be approximately 110 μm thick using an automated fluorescence microscope to find the two focal planes containing either the embedded patterns or the glass substrate and calculating the distance between them). The bottom of the modelled substrate was assigned a fixed boundary condition (displacement = 0) and tangential forces ranging from 1 to 250 nN were applied to 5 μm × 10 μm regions on the top surface of the modelled substrate at the vertices of the pattern. To compute the pattern displacement due to an applied force, maximum values of the in-plane deformation were calculated on the four edges of

the pattern region. Due to symmetry, the points of maximum displacement were located at the centre points of each terminal boundary—the same locations as where the imaging analysis algorithm measures displacement.

AQ34

AQ35

For this model, the key assumptions of elasticity and linearity hold. Relaxation of contracted cells with the myosin inhibitor blebbistatin results in patterns returning to their unperturbed size and shape, suggesting elastic behaviour and a lack of plastic deformation (Supplementary Video 3). Additionally, previous work has demonstrated that PDMS behaves as a linearly elastic material under quasi-static loading conditions[52]. Finally, the observed deflections of the substrate are small compared with the size of the substrate so we do not expect significant departures from linearity. This model is similar to that employed by ref. [14], although our system allows for direct measurement of substrate deflection, removing the need for including the cell in the simulation.

Macrophage drug panel

Experimental

Methods for cell culture and substrate preparation were identical to our earlier macrophage experiments, but using exclusively hIgG patterns. Chloroquine, CAL-101 and cytochalasin D were dissolved in medium or DMSO and delivered to FLECS plate wells at final concentrations of 0.1, 1 and 10 μM either before the macrophages were seeded or after they had maintained adhesion to the patterns for 24 h. When delivery was before macrophage seeding, imaging was performed 24 h later. When it was after, imaging was performed 15 min after addition of the drug.

Analysis

Since an inactive sub-population of macrophages was prevalent in the overall population, we fitted a mixed Gaussian curve to each distribution using the open-source MATLAB function *peakfit.m* developed by T. O'Haver (University of Maryland). To obtain the best fit, the two Gaussian widths were restricted to a minimum of 1, but were otherwise unconstrained. In each case (except for pre-treatment with cytochalasin D), two Gaussians were clearly identified in the best fit, representing the inactive (near-zero contraction) and active populations. Overall curve-fit error rates were low at <7% and R^2 values were all >0.93. The central positions of the Gaussians, representing the active populations, were used for

quantifying the contractile capability of the macrophages following treatment with vehicle or drug.

AQ36

Cardiac myocyte experiments

Cell culture and imaging

Freshly isolated neonatal rat ventricular myocytes were a generous gift from J. Zixi Lee and Y. Wang. Immediately after isolation, the cells were brought in suspension in DMEM media supplemented with 1% insulin-transferrin-sodium selenite, and seeded onto samples patterned either with fibronectin/fibrinogen cross-shaped patterns (50 μm diagonal and 10 μm thickness) or 200 μm^2 rod-shaped patterns with a 7:1 length ratio. Approximately 6 h after seeding, spontaneous beating was observed in a fraction of cells. Patterns contracted by beating cells were imaged using fast time-lapsed imaging with short exposure times (for example, 100 ms) enabling real-time observations of the contractions.

AQ37

Electrical stimulation

To pace the cells, an assembly was created based on previous work[53]. Briefly, carbon rods were placed in parallel 5 cm in a petri dish and held in place using cured Sylgard 184. Platinum wire was wrapped around each carbon rod and connected to either electrode on a Grass Instrument SD9 pulse generator. Pulse widths of 10 μs and 80 V were applied at 1 or 2 Hz to pace cardiac cells adhered to patterns placed inside the petri dish.

AQ38

Life Sciences Reporting Summary

Further information on experimental design is available in the Life Sciences Reporting Summary.

Code availability

The MATLAB computer code used to evaluate micropattern displacements and calcium dye intensity is provided as Supplementary Information.

Data availability

All data supporting the findings of this study are available within the paper and its Supplementary Information. Source data for most plots are available on Figshare through the following DOIs:

https://doi.org/10.6084/m9.figshare.5717842.v1

https://doi.org/10.6084/m9.figshare.5717845.v1

https://doi.org/10.6084/m9.figshare.5717839.v1

Source data of large single-cell-contraction distributions are stored in .mat files and are available from the corresponding author upon reasonable request.

Electronic supplementary material

Supplementary information accompanies this paper at https://doi.org/10.1038/s41551-018-0193-2.

Publisher's note: Springer Nature remains neutral with regard to jurisdictional claims in published maps and institutional affiliations.

Acknowledgements

The work was supported by the National Institutes of Health Director's New Innovator Award 1DP2OD007113, the David and Lucile Packard Fellowship and the National Institutes of Health/National Institute of Biomedical Imaging and Bioengineering R21 Award 1R21EB024081-01. The authors thank C. Walthers for providing the primary mouse intestinal SMCs used in the Supplementary Videos, Y. Wang and J. Zixi Lee for providing the neonatal rat ventricular myocytes, and O. Adeyiga for performing bloods draws over the course of six months to facilitate primary macrophage culture. All microfabrication steps were completed using equipment provided by the Integrated Systems Nanofabrication Cleanroom at the California NanoSystems Institute at the University of California, Los Angeles.

AQ39

AQ40

AQ41

Author contributions

P.T., D.D.C. and I.P. conceived the methods. I.P., R.D., P.O.S., S.L.M., R.A.P., C.J.K.-W. and D.D.C. designed the experiments. I.P. performed all the experiments, developed the multi-well embodiment, optimized the protocols and wrote the image

analysis software. D.B. assisted with the substrate preparation and macrophage differentiation procedures. L.W. assisted with the substrate preparation. R.K.T. maintained the chimeric antibody stocks. S.L.M. supplied all the chimeric antibodies. J.L. constructed the finite element method model. R.D. supplied the HTS equipment for dose-response experiments and provided extensive guidance and technical advice on HTS procedures and developing the multi-well plate embodiment. B.F. assisted with the HTS equipment and drug administration. W.F.J. maintained the donor HASM cells. P.O.S. performed the MDC differentiation and advised the experimental procedures. I.P., R.D., P.O.S., S.L.M., R.A.P., C.J.K.-W. and D.D.C. interpreted the results. I.P. and D.D.C. wrote the manuscript. R.D., P.O.S., S.L.M., R.A.P. and C.J.K.-W. helped revise the manuscript.

AQ42

AQ43

AQ44

Competing interests I.P., P.T. and D.D.C. are named inventors on a patent application by the University of California, Los Angeles that covers the technology described in this study. I.P., R.D. and D.D.C. have a financial interest in Forcyte Biotechnologies, which aims to commercialize FLECS technology.

Supplementary information

Supplementary Information Life Sciences Reporting Summary

Supplementary figures, tables and video captions.

Supplementary Text

MATLAB computer code used to evaluate micropattern displacements and calcium dye intensity.

Videos

Supplementary Video 1

Fibronectin–fibrinogen patterns created using our sacrificial dextran method.

Supplementary Video 2

A second example of fibronectin–fibrinogen patterns created using the sacrificial dextran method.

Supplementary Video 3

Patterns contracted by adhered HeLa cells relax after the addition of the myosin inhibitor blebbistatin. Time-lapsed video.

Supplementary Video 4

HASM cells treated with 1 μM bradykinin contract significantly beyond tonic levels within 30 minutes.

Supplementary Video 5

HASM cells treated with 100 nM endothelin-1 contract significantly beyond tonic levels within 30 minutes.

Supplementary Video 6

Visualization of calcium flux within HASM cells seeded on arrays of FLECS micropatterns after the addition of Hist.

Supplementary Video 7

Time-lapsed video of human monocyte-derived macrophages engaged in frustrated phagocytosis of an IgG-opsonized patterned surface.

Supplementary Video 8

Representative video (real time) of a phasically contracting neonatal rat ventricular myocyte.

Supplementary Video 9

Representative video (real time) of a pattern phasically contracted by an adhered and spontaneously beating neonatal rat ventricular myocyte.

Supplementary Video 10

Representative video (real time) of a pattern phasically contracted by an adhered and beating neonatal rat ventricular myocyte paced with pulsed electric fields at frequencies of 1 Hz and 2 Hz.

Supplementary Video 11

Fibronectin–fibrinogen patterns created using adsorption rather than our sacrificial dextran method. Time-lapse video.

Supplementary Video 12

Second example of fibronectin–fibrinogen patterns created using adsorption rather than our sacrificial dextran method. Time-lapse video.

References

1. Discher, D. E., Janmey, P. & Wang, Y.-L. Tissue cells feel and respond to the stiffness of their substrate. *Science* **310**, 1139–1143 (2005).

2. Fournier, M. F., Sauser, R., Ambrosi, D., Meister, J.-J. & Verkhovsky, A. B. Force transmission in migrating cells. *J. Cell Biol.* **188**, 287–297 (2010).

3. Burton, K. & Taylor, D. L. Traction forces of cytokinesis measured with optically modified elastic substrata. *Nature* **385**, 450–454 (1997).

4. Evans, E., Leung, A. & Zhelev, D. Synchrony of cell spreading and contraction force as phagocytes engulf large pathogens. *J. Cell Biol.* **122**, 1295–1300 (1993).

5. Hall, C. N. et al. Capillary pericytes regulate cerebral blood flow in health and disease. *Nature* **508**, 55–60 (2014).

6. Pelaia, G. et al. Molecular mechanisms underlying airway smooth muscle contraction and proliferation: implications for asthma. *Respir. Med.* **102**, 1173–1181 (2008).

7. Yemisci, M. et al. Pericyte contraction induced by oxidative-nitrative stress impairs capillary reflow despite successful opening of an occluded cerebral artery. *Nat. Med.* **15**, 1031–1037 (2009).

8. Huang, X. et al. Relaxin regulates myofibroblast contractility and protects against lung fibrosis. *Am. J. Pathol.* **179**, 2751–2765 (2011).

9. Valencia, A. M. J. et al. Collective cancer cell invasion induced by coordinated contractile stresses. *Oncotarget* **6**, 43438–43451 (2015).

10. Gupta, S., Nahas, S. J. & Peterlin, B. L. Chemical mediators of migraine: preclinical and clinical observations. *Headache* **51**, 1029–1045 (2011).

11. Munevar, S., Wang, Y. & Dembo, M. Traction force microscopy of migrating normal and H-ras transformed 3T3 fibroblasts. *Biophys. J.* **80**, 1744–1757 (2001).

12. Park, C. Y. et al. High-throughput screening for modulators of cellular contractile force. *Integr. Biol. (Camb.)* **7**, 1318–1324 (2015).

13. Tan, J. L. et al. Cells lying on a bed of microneedles: an approach to isolate mechanical force. *Proc. Natl Acad. Sci. USA* **100**, 1484–1489 (2003).

14. Oakes, P. W., Banerjee, S., Marchetti, M. C. & Gardel, M. L. Geometry regulates traction stresses in adherent cells. *Biophys. J.* **107**, 825–833 (2014).

15. Ricart, B. G., Yang, M. T., Hunter, C. A., Chen, C. S. & Hammer, D. A. Measuring traction forces of motile dendritic cells on micropost arrays. *Biophys. J.* **101**, 2620–2628 (2011).

16. Legant, W. R. et al. Multidimensional traction force microscopy reveals out-of-plane rotational moments about focal adhesions. *Proc. Natl Acad. Sci. USA* **110**, 881–886 (2013).

17. Polacheck, W. J. & Chen, C. S. Measuring cell-generated forces: a guide to the available tools. *Nat. Methods* **13**, 415–423 (2016).

18. Myers, D. R. et al. Single-platelet nanomechanics measured by high-throughput cytometry. *Nat. Mater.* **16**, 230–235 (2017).

19. Tseng, Q. et al. A new micropatterning method of soft substrates reveals that different tumorigenic signals can promote or reduce cell contraction levels. *Lab Chip* **11**, 2231–2240 (2011).

20. Rape, A., Guo, W. & Wang, Y. The regulation of traction force in relation to cell shape and focal adhesions. *Biomaterials* **32**, 2043–2051 (2011).

21. Wang, N., Ostuni, E., Whitesides, G. M. & Ingber, D. E. Micropatterning tractional forces in living cells. *Cell Motil. Cytoskeleton* **52**, 97–106 (2002).

22. Fu, J. et al. Mechanical regulation of cell function with geometrically modulated elastomeric substrates. *Nat. Methods* **7**, 733–736 (2010).

23. Kim, H. R., Appel, S., Vetterkind, S., Gangopadhyay, S. S. & Morgan, K. G. Smooth muscle signalling pathways in health and disease. *J. Cell. Mol. Med.* **12**, 2165–2180 (2008).

24. Limouze, J., Straight, A. F., Mitchison, T. & Sellers, J. R. Specificity of blebbistatin, an inhibitor of myosin II. *J. Muscle Res. Cell Motil.* **25**, 337–341 (2004).

AQ45

25. Straight, A. F. et al. Dissecting temporal and spatial control of cytokinesis with a myosin II inhibitor. *Science* **299**, 1743–1747 (2003).

26. An, S. S. et al. An inflammation-independent contraction mechanophenotype of airway smooth muscle in asthma. *J. Allergy Clin. Immunol.* **138**, 294–297.e4 (2016).

27. Herington, J. L. et al. High-throughput screening of myometrial calcium-mobilization to identify modulators of uterine contractility. *PLoS ONE* **10**, e0143243 (2015).

28. Wertek, F. & Xu, C. Digital response in T cells: to be or not to be. *Cell Res.* **24**, 265–266 (2014).

29. McNally, A. K., Jones, J. A., Macewan, S. R., Colton, E. & Anderson, J. M. Vitronectin is a critical protein adhesion substrate for IL-4-induced foreign body giant cell formation. *J. Biomed. Mater. Res. A* **86**, 535–543 (2008).

30. Labernadie, A., Thibault, C., Vieu, C., Maridonneau-Parini, I. & Charrière, G. M. Dynamics of podosome stiffness revealed by atomic force microscopy. *Proc. Natl Acad. Sci. USA* **107**, 21016–21021 (2010).

31. Gordon, S. & Taylor, P. R. Monocyte and macrophage heterogeneity. *Nat. Rev. Immunol.* **5**, 953–964 (2005).

32. Soon, C. F., Tee, K. S., Youseffi, M. & Denyer, M. C. T. Tracking traction force changes of single cells on the liquid crystal surface. *Biosensors (Basel)* **5**, 13–24 (2015).

33. Tsang, P. H., Li, G., Brun, Y. V., Freund, L. B. & Tang, J. X. Adhesion of single bacterial cells in the micronewton range. *Proc. Natl Acad. Sci. USA* **103**, 5764–5768 (2006).

34. Hind, L. E., Dembo, M. & Hammer, D. A. Macrophage motility is driven by frontal-towing with a force magnitude dependent on substrate stiffness. *Integr. Biol. (Camb.)* **7**, 447–453 (2015).

35. Goh, Y. S. et al. Human IgG isotypes and activating Fcγ receptors in the interaction of *Salmonella enterica* serovar Typhimurium with phagocytic cells. *Immunology* **133**, 74–83 (2011).

36. Kaplan, G. Differences in the mode of phagocytosis with Fc and C3 receptors in macrophages. *Scand. J. Immunol.* **6**, 797–807 (1977).

37. Hackam, D. J., Rotstein, O. D. & Grinstein, S. Phagosomal acidification mechanisms and functional significance. *Adv. Cell. Mol. Biol. Membr. Organelles* **5**, 299–319 (1999).

38. Schlam, D. et al. Phosphoinositide 3-kinase enables phagocytosis of large particles by terminating actin assembly through Rac/Cdc42 GTPase-activating proteins. *Nat. Commun.* **6**, 8623 (2015).

39. Beemiller, P. et al. A Cdc42 activation cycle coordinated by PI 3-kinase during Fc receptor-mediated phagocytosis. *Mol. Biol. Cell* **21**, 470–480 (2010).

40. Papakonstanti, E. A. et al. Distinct roles of class IA PI3K isoforms in primary and immortalised macrophages. *J. Cell Sci.* **121**, 4124–4133 (2008).

41. Castellano, F., Montcourrier, P. & Chavrier, P. Membrane recruitment of Rac1 triggers phagocytosis. *J. Cell Sci.* **113**, 2955–2961 (2000).

42. Massol, P., Montcourrier, P., Guillemot, J.-C. & Chavrier, P. Fc receptorâ€ mediated phagocytosis requires CDC42 and Rac1. *EMBO J.* **17**, 6219–6229 (1998).

43. Ganesan, L. P. et al. The serine/threonine kinase Akt promotes Fcγ receptor-mediated phagocytosis in murine macrophages through the activation of p70S6 kinase. *J. Biol. Chem.* **279**, 54416–54425 (2004).

44. Papakonstanti, E. A., Ridley, A. J. & Vanhaesebroeck, B. The p110δ isoform of PI 3-kinase negatively controls RhoA and PTEN. *EMBO J.* **26**, 3050–3061 (2007).

45. Swinney, D. C. Phenotypic vs. target-based drug discovery for first-in-class medicines. *Clin. Pharmacol. Ther.* **93**, 299–301 (2013).

46. Tseng, P., Pushkarsky, I. & Carlo, D. D. Metallization and biopatterning on ultra-flexible substrates via dextran sacrificial layers. *PLoS ONE* **9**, e106091 (2014).

47. Panettieri, R. A., Murray, R. K., DePalo, L. R., Yadvish, P. A. & Kotlikoff, M. I. A human airway smooth muscle cell line that retains physiological responsiveness. *Am. J. Physiol.* **256**, C329–C335 (1989).

48. Koziol-White, C. J. et al. Inhibition of PI3K promotes dilation of human small airways in a rho kinase-dependent manner. *Br. J. Pharmacol.* **173**, 2726–2738 (2016).

AQ46

49. Yoo, E. J. et al. Gα12 facilitates carbachol-induced shortening in human airway smooth muscle by modulating phosphoinositide 3-kinase-mediated activation in a RhoA-dependent manner. *Br. J. Pharmacol.* **174**, 4383–4395 (2017).

AQ47

50. Morrison, S. L., Johnson, M. J., Herzenberg, L. A. & Oi, V. T. Chimeric human antibody molecules: mouse antigen-binding domains with human constant region domains. *Proc. Natl Acad. Sci. USA* **81**, 6851–6855 (1984).

51. Zhuang, P. et al. Characterization of the denaturation and renaturation of human plasma vitronectin II. Investigation into the mechanism of formation of multimers. *J. Biol. Chem.* **271**, 14333–14343 (1996).

52. Vanlandingham, M. R., Chang, N.-K., Drzal, P. L., White, C. C. & Chang, S.-H. Viscoelastic characterization of polymers using instrumented indentation. I. Quasi-static testing. *J. Polym. Sci. B Polym. Phys.* **43**, 1794–1811 (2005).

53. Tandon, N. et al. Electrical stimulation systems for cardiac tissue engineering. *Nat. Protoc.* **4**, 155–173 (2009).

54. Beussman, K. M. et al. Micropost arrays for measuring stem cell-derived cardiomyocyte contractility. *Methods* **94**, 43–50 (2016).

55. Cheng, Q., Sun, Z., Meininger, G. & Almasri, M. PDMS elastic micropost arrays for studying vascular smooth muscle cells. *Sens. Actuators B Chem.* **188**, 1055–1063 (2013).

56. Munevar, S., Wang, Y. & Dembo, M. Traction force microscopy of migrating normal and H-ras transformed 3T3 fibroblasts. *Biophys. J.* **80**, 1744–

1757 (2001).

57. Wu, H. et al. Epigenetic regulation of phosphodiesterases 2A and 3A underlies compromised β-adrenergic signaling in an iPSC model of dilated cardiomyopathy. *Cell Stem Cell* **17**, 89–100 (2015).

58. Del Álamo, J. C. et al. Three-dimensional quantification of cellular traction forces and mechanosensing of thin substrata by Fourier traction force microscopy. *PLoS ONE* **8**, e69850 (2013).

59. Plotnikov, S. V., Pasapera, A. M., Sabass, B. & Waterman, C. M. Force fluctuations within focal adhesions mediate ECM-rigidity sensing to guide directed cell migration. *Cell* **151**, 1513–1527 (2012).

60. Goedecke, N., Bollhalder, M., Bernet, R., Silvan, U. & Snedeker, J. Easy and accurate mechano-profiling on micropost arrays. *J. Vis. Exp.* **2015**, e53350 (2015).
AQ48

61. ToliÄ‡-Nørrelykke, I. M. & Wang, N. Traction in smooth muscle cells varies with cell spreading. *J. Biomech.* **38**, 1405–1412 (2005).

62. Liu, K. et al. Improved-throughput traction microscopy based on fluorescence micropattern for manual microscopy. *PLoS ONE* **8**, e70122 (2013).

63. Colin-York, H. et al. Super-resolved traction force microscopy (STFM). *Nano Lett.* **16**, 2633–2638 (2016).

64. Murrell, M., Oakes, P. W., Lenz, M. & Gardel, M. L. Forcing cells into shape: the mechanics of actomyosin contractility. *Nat. Rev. Mol. Cell Biol.* **16**, 486–498 (2015).

65. Basu, R. et al. Cytotoxic T cells use mechanical force to potentiate target cell killing. *Cell* **165**, 100–110 (2016).